Remote Sensing of Environment 316 (2025) 114482

Contents lists available at ScienceDirect

Remote Sensing of Environment

journal homepage: www.elsevier.com/locate/rse

# First retrieval of 24-hourly 1-km-resolution gapless surface ozone ($O_3$) from space in China using artificial intelligence: Diurnal variations and implications for air quality and phytotoxicity

Fan Cheng [a], Zhanqing Li [b,*], Zeyu Yang [a], Ruohan Li [c], Dongdong Wang [c], Aolin Jia [d], Ke Li [e], Bin Zhao [f,g], Shuxiao Wang [f,g], Dejia Yin [f,g], Shengyue Li [f,g], Wenhao Xue [h], Maureen Cribb [b], Jing Wei [b,*]

[a] College of Global Change and Earth System Science, Faculty of Geographical Science, Beijing Normal University, Beijing, China
[b] Department of Atmospheric and Oceanic Science, Earth System Science Interdisciplinary Center, University of Maryland, College Park, MD, USA
[c] Department of Geographical Sciences, University of Maryland, College Park, MD, USA
[d] Department of Environment Research and Innovation, Luxembourg Institute of Science and Technology (LIST), Belvaux, Luxembourg
[e] Jiangsu Key Laboratory of Atmospheric Environment Monitoring and Pollution Control, Collaborative Innovation Center of Atmospheric Environment and Equipment Technology, School of Environmental Science and Engineering, Nanjing University of Information Science and Technology, Nanjing, China
[f] State Key Joint Laboratory of Environmental Simulation and Pollution Control, School of Environment, Tsinghua University, Beijing, China
[g] State Environmental Protection Key Laboratory of Sources and Control of Air Pollution Complex, Beijing 100084, China
[h] School of Economics, Qingdao University, Qingdao, China

ARTICLE INFO

Edited by Marie Weiss

*Keywords:*
Diurnal $O_3$ variations
(explainable) artificial intelligence
SHAP
Air quality
Vegetation phytotoxicity

ABSTRACT

Surface ozone ($O_3$) is a critical ambient pollutant that poses significant risks to both human health and ecosystems. However, there is a scarcity of high-spatial-resolution hourly surface $O_3$ data, which is crucial for understanding its diurnal variations. In this study, we employed a best-performing spatiotemporal artificial intelligence (AI) model to estimate 24-hourly 1-km-resolution surface $O_3$ concentrations across China, incorporating key photochemical processes responsible for $O_3$ formation. Our model effectively captured diurnal $O_3$ patterns, achieving average sample-based cross-validated coefficients of determination (root-mean-square errors) of 0.89 (16.35 μg/m$^3$) for the full day (00:00–23:00 LT), 0.92 (15.72 μg/m$^3$) during daytime (08:00–20:00 LT), and 0.82 (16.97 μg/m$^3$) at nighttime (20:00–08:00 LT). Typically, surface $O_3$ levels increase after sunrise, peak around 15:00 LT, and decrease overnight, with a diurnal variation magnitude of 62 % relative to the mean level. During the daytime, we found that solar radiation (in the ultraviolet and shortwave spectra) and surface temperature explained over 42 % of the diurnal variation, while nighttime $O_3$ levels were mainly influenced by tropospheric nitrogen dioxide (16 %), temperature (13 %), and relative humidity (12 %). In 2019, approximately 61 %, 98 %, and 100 % of populated areas in China experienced $O_3$ exposure risks for at least one day, with maximum daily 8-h average (MDA8) $O_3$ levels exceeding 160, 120, and 100 μg/m$^3$, respectively. Additionally, around 70 %, 82 %, and 100 % of vegetated areas exceeded the three minimum critical thresholds for cumulative hourly $O_3$ exposure, as indicated by the SUM06, W126, and AOT40 indices, respectively. Notably, gross primary productivity (GPP) was the most sensitive indicator of $O_3$ pollution across various vegetation types, showing a strong negative correlation with AOT0 ($R = -0.43$ to $-0.59$, $p < 0.001$).

## 1. Introduction

Ozone ($O_3$) is a crucial trace gas in the atmosphere, primarily distributed in the stratosphere. It efficiently absorbs ultraviolet (UV) radiation, shielding virtually all Earth's living organisms and ecosystems from harmful effects. However, $O_3$ in the lower troposphere, particularly near the ground, damages human health and suppresses plant growth. As a greenhouse gas, it exerts radiative effects that lead to lower evaporation rates and relative humidity, altered precipitation patterns, and changes in atmospheric circulation (Allen et al., 2012; Fu and Tian,

* Corresponding authors.
*E-mail addresses:* zhanqing@umd.edu (Z. Li), weijing@umd.edu (J. Wei).

https://doi.org/10.1016/j.rse.2024.114482
Received 31 October 2023; Received in revised form 16 October 2024; Accepted 18 October 2024

2019; Lu et al., 2019; Stevenson et al., 2013). Being a primary air pollutant, its damage to human health is linked to various respiratory and cardiovascular diseases, such as kidney disease, circulatory disease, respiratory disease, and stroke (Brauer et al., 2016; Cai et al., 2023; Chen et al., 2023a; Lin et al., 2018; Niu et al., 2022). Its harmful impacts on vegetation lead to reductions in carbon assimilation by most plants (Fares et al., 2013), gross primary productivity (GPP) (Yue and Unger, 2014), crop yield (Lin et al., 2018), and thus the food supply (Wilkinson et al., 2012). When this highly reactive oxidant infiltrates leaves through stomata, the generation of additional reactive oxygen will trigger oxidative stress. Consequently, this hampers photosynthesis, impedes plant growth, and reduces yields (Ainsworth et al., 2012).

China, as one of the most populous countries with rapid development in the world, has suffered from significant air quality problems during the last four decades. In recent years, especially since 2013, China has enforced various strict air pollution control policies to significantly reduce anthropogenic pollutant emissions, leading to a notable improvement in air quality, with a large reduction (39 % during the period 2013–2020) in $PM_{2.5}$ concentrations (Wei et al., 2021). On the contrary, surface $O_3$ pollution has worsened seriously during the same period (Huang et al., 2019; Wang et al., 2020) at an average increasing rate of 2.49 $\mu g/m^3$/yr ($p < 0.001$). The area surpassing the daily standard [i.e., maximum daily average 8-h (MDA8) $O_3 = 160$ $\mu g/m^3$] has also expanded considerably (Wei et al., 2022a). Thus, more effective surface $O_3$ control measures in the future are urgently needed.

To address the escalating problem of surface $O_3$ pollution, continuously monitoring and ascertaining its mass concentration is imperative. Ground-based observations have high precision and reliability, enabling real-time monitoring of surface $O_3$ concentrations at specific sites. However, due to the uneven distribution of sites, achieving full coverage of $O_3$ monitoring remains a significant challenge. Chemical transport models, such as the Community Multiscale Air Quality (CMAQ) Modeling System, the Goddard Earth Observing System three-dimensional model of atmospheric chemistry (GEOS-Chem), and the Weather Research and Forecasting model coupled with chemistry (WRF-Chem), can simulate surface $O_3$ at a high temporal resolution (every one or several hours), but their accuracies are highly uncertain, and spatial resolutions are typically coarse, often at the degrees' level. As the resolution increases, computational costs rise drastically. In particular, surface $O_3$ from atmopspheric reanalysis products [e.g., Modern-Era Retrospective Analysis for Research and Applications, Version 2 (MERRA-2) and the European Centre for Medium-Range Weather Forecasts Reanalysis, Version 5 (ERA5)] have very large uncertainties in China compared with ground measurements [e.g., coefficient of determination ($R^2$) < 0.1 and root-mean-square error (RMSE) > 47 $\mu g/m^3$] (Hou et al., 2022; Hu et al., 2016; Qiao et al., 2019; Wang et al., 2015; Wei et al., 2022a). Satellite remote sensing can provide $O_3$ retrievals of total column amount and vertical profiles from a series of instruments, such as the Tropospheric Monitoring Instrument (TROPOMI) and the Ozone Monitoring Instrument (OMI), enabling us to monitor spatially continuous $O_3$ from space, together with other sources of data pertaining to surface $O_3$ (Chen et al., 2022a; Kang et al., 2021; Zhu et al., 2023).

Trace amounts of $O_3$ are affected by numerous other factors through complex relationships, making highly accurate retrievals using conventional statistical approaches challenging. In recent years, considerable efforts have thus been undertaken to obtain surface $O_3$ concentrations using machine-learning (ML) approaches (Capilla, 2016; Li et al., 2022; Li and Cheng, 2021; Ma et al., 2021; Song et al., 2022; Wang et al., 2022c). We, for example, have used advanced ML to develop a long-term surface $O_3$ dataset with high accuracy in China called ChinaHigh$O_3$ (Wei et al., 2022a) that has been widely adopted for tracking air pollution (Chen et al., 2022b; Xia et al., 2022) and used in many public health studies (Cai et al., 2023; Zhang et al., 2022). However, most prior studies, including ours, have mainly concentrated on the daily (MDA8) scale, with only a handful delving into the diurnal hourly scale. Zhang et al. (2023) adopted a bagged-tree model to generate hourly (09:00–16:00 LT) ground-level $O_3$ concentrations at a 5-km resolution over China by integrating the hourly Himawari-8 shortwave radiation product. Chen et al. (2023b) built a deep-learning (DL) model to acquire hourly (10:00–15:00 LT) 5-km surface $O_3$ concentrations from Himawari-8 top-of-the-atmosphere radiation. Wang et al. (2022b) explored a self-adaptive geospatially local categorical boosting approach for estimating hourly (09:00–18:00 LT) 2-km surface $O_3$ concentrations across China using Himawari-8 AHI brightness temperatures at multiple thermal infrared bands. However, these studies have only estimated hourly surface $O_3$ during the daytime (usually less than 10 h), failing to provide comprehensive 24-hourly coverage. 24-hourly data are of utmost importance for the calculation of not only air quality metrics like MDA8 but also $O_3$-exposure phytotoxicity indices, such as 12-h average surface $O_3$ concentrations (M12), Accumulation of surface $O_3$ concentrations without Threshold (AOT0), and SUM of surface $O_3$ concentrations $\geq$ 60 ppb (SUM06). Retrievals from most previous studies also have large data gaps due to the presence of clouds that handicaps optical satellite remote sensing, seriously limiting their applications.

For the first time, we attempt to derive *24-hourly 1-km-resolution gapless* surface $O_3$ concentrations across China using a best-performing model that makes use of ample satellite, ground, and model datasets pertinent to $O_3$, such as solar radiation and surface temperature retrievals from geostationary satellites, and many other factors influencing surface $O_3$ concentrations. The best-performing model was selected from 15 different tree-based ML and DL models, considering both model accuracy and efficiency. After being cross-validated independently against ground measurements, the $O_3$ products undergo a comprehensive analysis of spatial and temporal variations throughout both daytime and nighttime, with their driving factors identified and quantified by leveraging the eXplainable AI (XAI) - SHAP (SHapley Additive exPlanations) method. Additionally, using the 24-hourly data, we compute both the MDA8 $O_3$ and various $O_3$-exposure phytotoxicity indices and assess the short-term health risks of exposure to surface $O_3$ pollution, as well as the adverse impacts of $O_3$ pollution on vegetation.

## 2. Materials and methods

### 2.1. Data sources

#### 2.1.1. Surface $O_3$ observations

This study employs ground-level hourly $O_3$ observations ($\mu g/m^3$) from the Ministry of Ecology and Environment (MEE) in China from a total of 1605 monitoring stations in 2019 (Fig. S1), which are measured under room conditions (i.e., 298 K, 1013 hPa) (MEE, 2018). Any flagged invalid data are excluded. The conversion factor from $\mu g/m^3$ to ppb for $O_3$ is 0.467.

#### 2.1.2. Ancillary data for surface $O_3$ retrievals

Surface $O_3$, an important secondary pollutant in the atmosphere, is influenced by various factors during its formation and dissipation. Downward shortwave radiation (DSR) and land surface temperature (LST) play crucial roles in surface $O_3$ generation when the necessary substances for photochemical reactions, such as nitrogen oxides ($NO_x$) and volatile organic compounds (VOCs), are present. Here, hourly DSR and LST data from geostationary satellites are adopted by virtue of their high spatial and temporal variations. One-km-resolution DSR hourly data are obtained from the Geostationary-NASA Earth Exchange (GeoNEX) Level 2 product. This data was generated using a physically based look-up-table approach from data collected from new-generation geostationary Advanced Baseline Imager (ABI) and Advanced Himawari Imager (AHI) data (Li et al., 2023bLi et al., 2023b). Hourly LST data are derived from the Global Hourly All-sky-LST (GHA-LST) product with a downscaled 1-km resolution, generated by combining geostationary Earth orbit LST retrievals from the Copernicus Global Land Service (CGLS) and Moderate Resolution Imaging Spectroradiometer (MODIS)

MxD21 LST products. All-sky hourly LSTs are obtained using spatio-temporal assimilation to address satellite gaps (Jia et al., 2023). In addition to shortwave radiation, hourly UV radiation, including UVA (315–400 nm) and UVB (280–315 nm) sourced from Himawari-8 Level 3 photosynthetically active radiation (PAR) data (5-km resolution) with complete spatial coverage, has also been incorporated into our modeling, which plays a crucial role in impacting surface $O_3$ concentrations by catalyzing $O_3$ cycle initiation and controlling the $O_3$ generating rate (Barnard et al., 2003; Seinfeld and Pandis, 2016).

Satellite $O_3$ data and its precursor gases are highly correlated with surface $O_3$, providing valuable insights into $O_3$ formation sensitivity (Jin et al., 2017; Ren et al., 2022; Shah et al., 2020; Shen et al., 2019). Therefore, in the absence of geostationary satellite trace gas products, we include the TROPOMI tropospheric $O_3$, nitrogen dioxide ($NO_2$), and formaldehyde (HCHO) column products as important predictors into our model. In addition, we employ model-simulated spatially complete vertical columns from Copernicus Atmospheric Monitoring Service (CAMS) global reanalysis 4 (EAC4) multi-level data to fill the satellite gaps for each gas, utilizing the ML-based approach proposed in our previous study (Wei et al., 2022b). Key precursors for the formation of $O_3$ through photochemical reactions are $NO_x$, VOCs, and carbon monoxide (CO) (Wang et al., 2017a, 2022b). These anthropogenic emissions associated with human activities are obtained from the 1-km-resolution daily Air Benefit and Cost and Attainment Assessment System-Emission Inventory version 2.0 (ABaCAS-EI v2.0) dataset covering China (Li et al., 2023c). Population distribution data collected from the 1-km annual LandScan™ product is also employed.

Meteorological variables have significant and diverse impacts on air pollutants. Employed in our model are the following most influential ones from hourly ERA5 global reanalysis data: boundary layer height (BLH), relative humidity (RH), total precipitation (TP), surface pressure (SP), wind speed (WS), and wind direction (WD) (calculated from the u- and v-components of winds). The following variables attributed to surface conditions are also included: Shuttle Radar Topography Mission (SRTM) 90-m digital elevation model (DEM) and MODIS 1-km normalized difference vegetation index (NDVI) products. Altogether, we have gathered and employed a total of 19 variables for daytime and 16 for nighttime, with details provided in Table 1. All ancillary data are resampled (or reaggregated) to a 1-km resolution ($\approx 0.01^\circ \times 0.01^\circ$) using the bilinear interpolation method (Wei et al., 2023).

### 2.2. AI model establishment and selection

Besides exploiting various pertinent data sources, it is equally imperative to find the best model that can most effectively and efficiently extract any useful information for which AI has been proven to be most competent. To find the best-performing model, we applied 15 models, including nine tree-based ML and six DL models. For the tree-based ML ones, we chose the original Decision Tree (DT) and eight DT-derived ensemble-learning models consisting of multiple base models, falling into the two categories of bagging and boosting. Bagging models combine multiple independent base models through averaging or voting, including random forest (RF; Breiman, 2001) and extremely randomized trees (ET; Geurts et al., 2006). Boosting models entail iteratively constructing base models, with each model refining its performance based on the feedback from the preceding model, including Adaptive Boosting (AdaBoost), Gradient Boosting Decision Tree (GBDT), eXtreme Gradient Boosting (XGBoost), Light Gradient Boosting Machine (LightGBM), and Categorical Boosting (CatBoost). AdaBoost is one of the earliest techniques within the realm of boosting and assigns a higher weight to misclassified samples from the previous base model in each iteration (Freund and Schapire, 1997). GBDT constructs base models by progressively improving the loss function (Friedman, 2001), and both XGBoost and LightGBM are optimizations of the GBDT framework. XGBoost introduces training loss (second-order Taylor expansion) and regularization, while LightGBM applies a histogram optimization and gradient-based one-side sampling method (Chen and Guestrin, 2016; Ke et al., 2017). CatBoost is specially tailored for handling categorical features (Sagi and Rokach, 2018). Deep Forest (DF) is a hybrid model combining various tree-based models, rather than neurons, in each middle layer to handle non-linear relationships, allowing for the capture of complex data structures (Zhou and Feng, 2019).

For DL, we selected among the Multilayer Perceptron (MLP), Convolutional Neural Network (CNN), Long Short Term Memory (LSTM), Deep Belief Network (DBN), Deep Residual Network (ResNet), and Residual Next (ResNeXt) models. The MLP model serves as the fundamental neural network model capable of approximating complex nonlinear functions (Du et al., 2022). CNN is employed for grid-pattern data and relies on the core of the convolutional layer that involves a series of operations like convolution (Yamashita et al., 2018). We set the input channel of the first two-dimensional convolutional layer to 1 to input tabular data, and subsequently, each row of the table is introduced into the model for processing. LSTM is a special recurrent neural

**Table 1**
An overview of data sources employed in this study.

| Data | Full name of the variable | Abbreviation | Unit | Temporal resolution | Spatial resolution | Source |
|---|---|---|---|---|---|---|
| Ground truth | Ground-level $O_3$ measurements | – | $\mu g/m^3$ | 1 h | In situ | CNEMC |
| Solar radiation | Downward shortwave radiation | DSR | $W/m^2$ | 1 h | 1 km | GeoNEX |
| | Ultraviolet radiation A | UVA | $W/m^2$ | 1 h | 5 km | Himawari-8 |
| | Ultraviolet radiation B | UVB | $W/m^2$ | 1 h | 5 km | |
| Meteorological factors | Land surface temperature | LST | K | 1 h | 1 km | GHA-LST |
| | Boundary layer height | BLH | m | 1 h | 0.25° | ERA5 |
| | Relative humidity | RH | % | 1 h | 0.25° | |
| | Total precipitation | TP | mm | 1 h | 0.1° | ERA5-Land |
| | Surface pressure | SP | hPa | 1 h | 0.1° | |
| | Wind direction | WD | ° | 1 h | 0.1° | |
| | Wind speed | WS | m/s | 1 h | 0.1° | |
| Satellite gases | Tropospheric $O_3$ column | $TO_3$ | 1e15 molec/$cm^2$ | 1 day | $5 \times 3.5$ $km^2$ | TROPOMI |
| | Tropospheric $NO_2$ column | $TNO_2$ | 1e15 molec/$cm^2$ | 1 day | $5 \times 3.5$ $km^2$ | |
| | Tropospheric HCHO column | THCHO | 1e15 molec/$cm^2$ | 1 day | $5 \times 3.5$ $km^2$ | |
| Model gases | Tropospheric $O_3$ column | $MTO_3$ | kg $kg^{-1}$ | 3 h | 0.75° | CAMS EAC4 |
| | Tropospheric $NO_2$ column | $MTNO_2$ | kg $kg^{-1}$ | 3 h | 0.75° | |
| | Tropospheric HCHO column | MTHCHO | kg $kg^{-1}$ | 3 h | 0.75° | |
| Emission inventory | Nitrogen oxides | $NO_x$ | t | 1 day | 1 km | ABaCAS-EI |
| | Volatile organic compounds | VOCs | t | 1 day | 1 km | |
| | Carbon monoxide | CO | t | 1 day | 1 km | |
| Other factors | Digital elevation model | DEM | m | – | 90 m | SRTM |
| | Population | POP | people | 1 year | 1 km | LandScan™ |
| | Normalized difference vegetation index | NDVI | – | 16 day | 1 km | MOD13A2 |

network that effectively handles dependencies over long periods by using gate functions in its cell structure (Yu et al., 2019). In the current study, we adjust the sequence length to 1 to make the model compatible with tabular data, which does not incorporate time series information (Lei et al., 2022; Wang et al., 2022a; Zhang et al., 2024). DBN is a multi-layered neural network containing multiple restricted Boltzmann machines (Hinton et al., 2006). ResNet is designed to address network degradation issues in deeper neural networks by using shortcut connections to learn the residual between desired and current outputs of a specific layer, alleviating problems like gradient disappearance and network degradation (He et al., 2015). ResNeXt is an upgraded version of ResNet that introduces a novel building block called "cardinality bottleneck" (Xie et al., 2017). The abovementioned total of 15 AI models, each run separately, are adopted here to identify a best-performing model for retrieving hourly surface $O_3$ by comparing their accuracies and efficiencies using the same hourly training and validation datasets. Tables S1 and S2 provide details about all main parameters set in our selected AI models, including input data, number of layers, training parameterizations, batch size, and learning rate. In this study, we trained the models separately for different hours to address specific biases at certain times.

Previous studies have indicated that incorporating spatiotemporal factors can enhance the accuracy of a model in predicting air pollutants, considering their significant spatiotemporal continuity (Li et al., 2017; Wei et al., 2021). Consequently, here, a novel technique that assigns weighted effects based on polar coordinates with multidimensions is employed to compute the spatiotemporal factors (Sun et al., 2022; Wei et al., 2023), leading to the new extended 4-Dimensional Space-Time AI (4D-STAI) model. Spatial information is described within Euclidean space utilizing spherical coordinates (Eqs. 1–3), and temporal information is represented using three helix-shaped trigonometric vectors (Eqs. 4–6), encompassing both diurnal variations and seasonal cycles of air pollution.

$$S_1 = sin\left(2\pi\frac{Lon}{360}\right) \tag{1}$$

$$S_2 = cos\left(2\pi\frac{Lon}{360}\right)sin\left(2\pi\frac{Lat}{180}\right) \tag{2}$$

$$S_3 = cos\left(2\pi\frac{Lon}{360}\right)cos\left(2\pi\frac{Lat}{180}\right) \tag{3}$$

$$T_1 = \frac{DOY}{N} \tag{4}$$

$$T_2 = cos\left(2\pi\frac{DOY}{N}\right) \tag{5}$$

$$T_3 = sin\left(2\pi\frac{DOY}{N}\right) \tag{6}$$

where *Lon* signifies the longitude of each grid, and *Lat* signifies the latitude; *N* indicates a year's number of days in total (365 for the year 2019); and *DOY* refers to the day of the year.

### 2.3. Validation and analysis methods

Similar to many previous studies (Di et al., 2017; Kang et al., 2021; Wang et al., 2021; Zhan et al., 2018), the 10-fold cross-validation (10-CV) method is utilized for assessing and comparing the performance of the model, performed at the sample-based (out-of-sample), station-based (out-of-station), and block-based (out-of-block) levels. Sample CV is segregated according to all training data samples to evaluate the model's overall accuracy, while station CV is divided based on ground-based monitors to measure the spatial prediction accuracy (Li et al., 2017; Wei et al., 2022a). Block CV follows a procedure similar to the station CV but utilizes grid cells of $0.1^\circ \times 0.1^\circ$, comprising a total of 974 blocks covering China. This approach enables us to evaluate the model accuracy in predicting air pollutant concentrations in new spatial regions lacking ground-based observations (Yu et al., 2023). These three methods involve randomly dividing the entire dataset into 10 subsets. In each iteration, the model is trained on nine data subsets, with the rest for testing. This process runs in turn for 10 iterations, ensuring that all data participate in the model validation process (Rodriguez et al., 2010).

Surface $O_3$ concentrations are affected by diverse factors, as stated before, all of which exhibit variations across time and space. To comprehend the factors driving diurnal fluctuations in surface $O_3$ levels, we employed the XAI methodology. The game-theoretic SHAP approach is applied to explain the model output. Specifically, SHAP quantifies the significance of a feature by contrasting the predictions of the model when including and excluding that particular feature (Lundberg et al., 2020; Wei et al., 2024). We thus assess the importance of all variables for each hour using SHAP's TreeExplainer. Fig. 1 shows the flowchart of retrieving 24-hourly gapless surface $O_3$ concentrations in our study.

### 2.4. $O_3$ phytotoxicity indices

Many studies have shown that surface $O_3$ is a notable stressor in natural ecosystems, mainly affecting soil, biota, and ecological processes (Ainsworth et al., 2012; Kangasjarvi et al., 2005; Super et al., 2015). We have chosen various $O_3$ phytotoxicity indices to investigate how vegetation responds to damage caused by surface $O_3$ exposure. MX refers to the hourly average value of $O_3$ ($H_{O_3}$) within the specified period X, where M7 refers to the mean 7-h $O_3$ concentration between 09:00–16:00 LT, and M12 refers to the mean 12-h $O_3$ concentration between 08:00–20:00 LT, which mainly reflects the effects of $O_3$ levels on vegetation growth (Tong et al., 2009). This is expressed as

$$M7 = \frac{1}{n}\sum_{i=1}^{n}\left[H_{O_3}\right]_i \ (9 \le i < 16) \tag{7}$$

$$M12 = \frac{1}{n}\sum_{i=1}^{n}\left[H_{O_3}\right]_i \ (8 \le i < 20) \tag{8}$$

where the *i* represents the hour in local time, ranging from 0 to 23.

Fuhrer et al. (1997) and Grünhage et al. (1999) proposed the AOTX index representing the sum of hourly $O_3$ mixing ratios exceeding a threshold value (X ppb) between 06:00–21:00 LT. AOT0 refers to AOTX when no threshold value is set (Eq. 9), and AOT40 represents AOTX when the threshold value is set to 40 ppb (Eq. 10). AOT0 and AOT40 are usually used to measure the severity of vegetation damage caused by surface $O_3$ exposure. Generally, AOT40 is effective for assessing $O_3$ damage in highly polluted areas but may be less useful in regions with lower pollution levels. By contrast, AOT0 is more effective across a broader range of pollution levels due to the retention of lower $O_3$ levels. To assess the extent of $O_3$ phytotoxicity, we use the maximum values of AOT0 and AOT40 over three consecutive months from April to September as annual results (Hayes and Bangor, 2017). Additionally, AOT40 causes damage to vegetation when it exceeds the thresholds of 3 ppm for agricultural crops and semi-natural vegetation, 5 ppm for forest trees, and 6 ppm for horticultural crops (Hayes and Bangor, 2017).

$$AOT0 = \sum_{i=1}^{n}\left[H_{O_3}\right]_i \ (6 \le i \le 20) \tag{9}$$

$$AOT40 = \sum_{i=1}^{n}\left[H_{O_3} - 40\right]_i \ for \ \left[H_{O_3}\right] > 40 \ ppb \ (6 \le i \le 20) \tag{10}$$

Heck and Cowling (1997) and Kohut (2007) introduced a SUM06 index representing the maximum cumulative value of hourly $O_3$ mixing ratios above 60 ppb during 8:00–20:00 LT over three consecutive months from April to October (Eq. 11). SUM06 is detrimental to vegetation when it exceeds the thresholds of 8–12 ppm for natural ecosystems, 10–16 ppm for tree seedings, and 15–20 ppm for crops (Heck and Cowling, 1997).

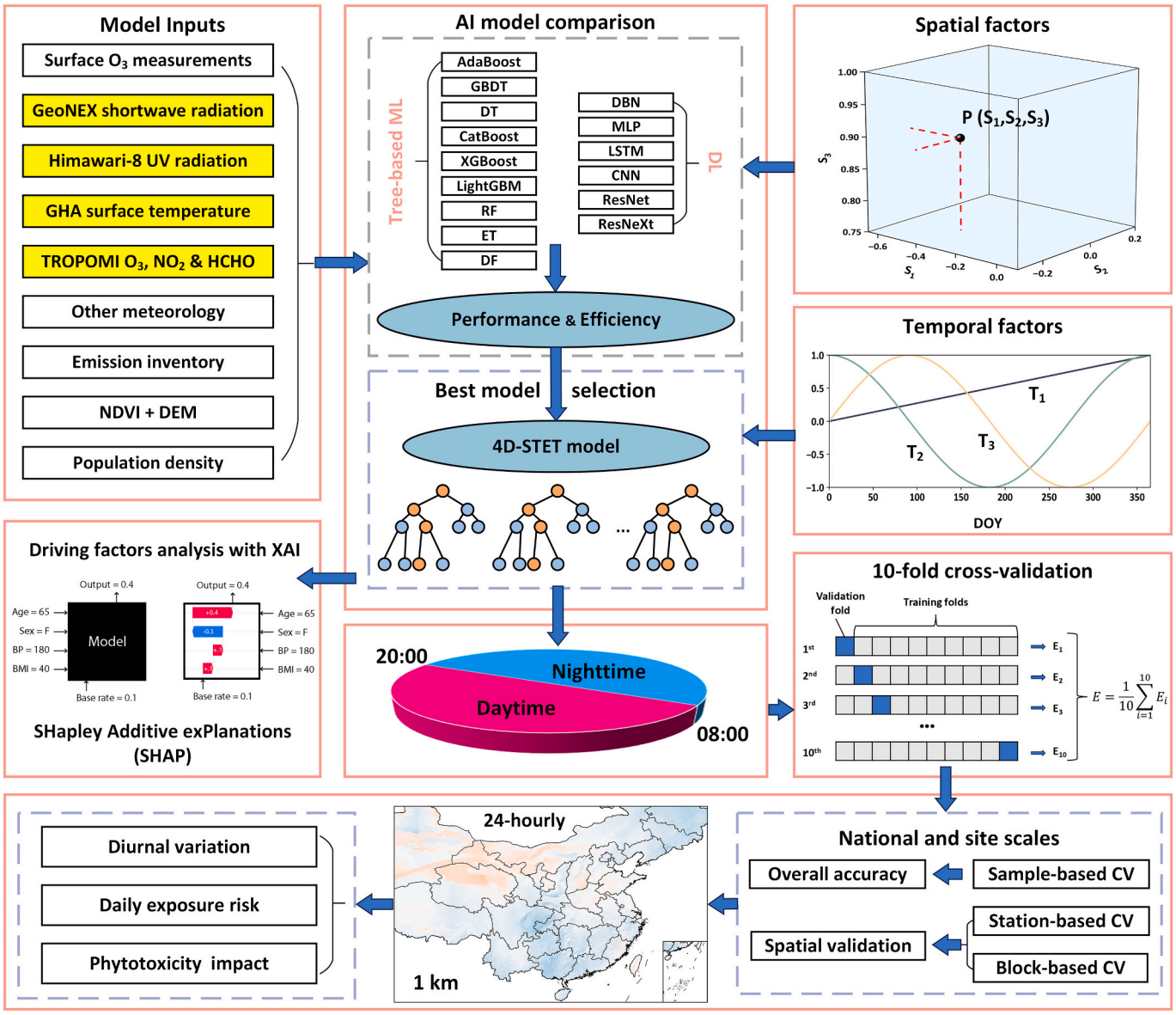


**Fig. 1.** Flowchart of how satellite-derived 24-hourly gapless 1-km-resolution surface $O_3$ levels are retrieved across China in this study using AI.

The W126 index is a sigmoidally weighted hourly concentration (Lefohn and Runeckles, 1987), calculated from the maximum of weighted cumulative values of hourly $O_3$ mixing ratios during 8:00–20:00 LT over three consecutive months from April to October (Eq. 12). It has a stronger response to elevated $O_3$ concentrations (Lefohn and Runeckles, 1987). W126 denotes damage to vegetation when it exceeds the specific thresholds of 5.9 ppm, 23.8 ppm, and 66.6 ppm for highly sensitive, moderately sensitive, and less sensitive species, respectively (Hayes and Bangor, 2017).

$$SUM06 = \sum_{i=1}^{n} \left[H_{O_3}\right]_i \; for \; \left[H_{O_3}\right] > 60 \; ppb \; (8 \le i < 20) \tag{11}$$

$$W126 = \sum_{i=1}^{n} \left[\frac{H_{O_3}}{1 + 4403e^{\left(-0.126 \times H_{O_3}\right)}}\right]_i \; (8 \le i < 20) \tag{12}$$

To analyze the $O_3$ phytotoxicity of different vegetation types, MODIS Land Use and Cover data were used to divide the land surface into three primary categories: forest, grassland, and cropland. We also assess and quantify the impacts of $O_3$ phytotoxicity on vegetation photosynthetic rate, growth situation, and yield by comparing six $O_3$ phytotoxicity indices (i.e., M7, M12, AOT0, AOT40, SUM06, and W126) with four vegetation abundance indices. The first, near-infrared reflectance of vegetation (NIRv), is calculated using the MOD13A2 16-day NDVI (1 km) and MCD43A4 1-day nadir reflectance (500 m) products (Badgley et al., 2017). The leaf area index (LAI) and fraction of PAR (FPAR) data (500 m) are collected from the MOD15A2H 8-day product. Gross primary production (GPP) data (0.072727° × 0.072727°) is generated from the Boreal Ecosystem Productivity Simulator model (He et al., 2021; Wang et al., 2017b).

## 3. Results and discussion

### 3.1. Model comparison and validation

#### 3.1.1. Optimal model

Table 2 compares the model performance and efficiency among the 15 AI models in estimating hourly surface $O_3$ concentrations in China, utilizing data samples from the same hour (i.e., 17:00 LT, number of samples, $N$ = 476,039). Most tree-based ML models have fast training speeds and consume relatively small amounts of memory, of which the AdaBoost model shows the poorest performance. The two original GBDT

**Table 2**
Performance and efficiency comparison of different 4-dimensional space-time (4D-ST) tree-based ML and DL models for estimating surface $O_3$ concentrations at 17:00 LT in China based on the out-of-sample CV approach.

| Category | Core model | $R^2$ | Slope | RMSE | MAE | Speed (s) | Memory (GB) |
|---|---|---|---|---|---|---|---|
| Tree-based machine learning | AdaBoost | 0.493 | 0.457 | 39.38 | 30.89 | 457.26 | 0.0015 |
| | DT | 0.745 | 0.867 | 28.85 | 19.16 | 11.80 | 0.0477 |
| | GBDT | 0.765 | 0.751 | 26.66 | 19.95 | 680.25 | 0.0008 |
| | CatBoost | 0.799 | 0.782 | 24.65 | 18.46 | 18.41 | 0.0456 |
| | XGBoost | 0.841 | 0.826 | 21.95 | 16.33 | 253.76 | 0.0240 |
| | RF | 0.877 | 0.838 | 19.45 | 13.71 | 332.14 | 5.9100 |
| | LightGBM | 0.905 | 0.887 | 17.00 | 12.27 | 29.95 | 0.0445 |
| | ET | 0.908 | 0.871 | 16.86 | 11.69 | 77.97 | 9.7143 |
| | DF | 0.911 | 0.903 | 16.41 | 11.45 | 14,945.32 | 17.4400 |
| Deep learning | MLP | 0.735 | 0.753 | 28.45 | 21.47 | 340.06 | 0.0911 |
| | DBN | 0.739 | 0.740 | 28.23 | 21.36 | 607.71 | 2.1617 |
| | ResNet | 0.808 | 0.771 | 24.32 | 18.06 | 2536.73 | 1.6808 |
| | CNN | 0.813 | 0.840 | 27.72 | 17.76 | 3627.53 | 1.8900 |
| | LSTM | 0.822 | 0.829 | 23.12 | 17.28 | 5776.59 | 0.0918 |
| | ResNeXt | 0.845 | 0.836 | 21.52 | 15.81 | 6819.31 | 1.9300 |

AdaBoost: Adaptive Boosting; DT: Decision Trees; GBDT: Gradient Boosting Decision Tree; CatBoost: Categorical Boosting; XGBoost: eXtreme Gradient Boosting; RF: Random Forest; LightGBM: Light Gradient Boosting Machine; ET: ExtraTrees; DF: Deep Forest; MLP: Multilayer Perceptron; DBN: Deep Belief Network; ResNet: Deep Residual Network; CNN: Convolutional Neural Network; LSTM: Long Short Term Memory; ResNeXt: ResNet Next.

and DT models have similar proficiencies in predicting hourly surface $O_3$, while the accuracies for their derived ensemble-learning models are improved, e.g., Catboost, XGBoost, RF, and LightGBM (e.g., CV-$R^2$ = 0.799, 0.841, 0.877, and 0.905, respectively). The ET model operates swiftly (78 s) and performs second only to DF (e.g., CV-$R^2$ = 0.908 versus 0.911). However, the ET model is faster than the DF model by ~192 times and uses about half as much memory. Among the six DL models, the MLP model performs the worst despite its fast training speed. The DBN model works better, with improved accuracy and minimal memory, but takes a significant amount of time (608 s). The ResNet model exhibits enhanced performance by incorporating residual structures to address issues such as gradient vanishing or explosion, thus delivering results efficiently. With continuous optimization in both model architectures and loss functions, the accuracy of surface $O_3$ estimates consistently increases, e.g., CV-$R^2$ = 0.813 and 0.845 for the CNN and ResNeXt models, respectively. However, their training speeds and memory requirements continue to increase. The traditional LSTM model (CV-$R^2$ = 0.822) is also not expected to be superior because it is susceptible to overfitting on training data (Yu et al., 2019). This model also encounters varnishing or exploding gradients when confronted with training data containing longer-term dependencies (Pascanu et al., 2013). Interestingly, most DL models perform not as accurately as and

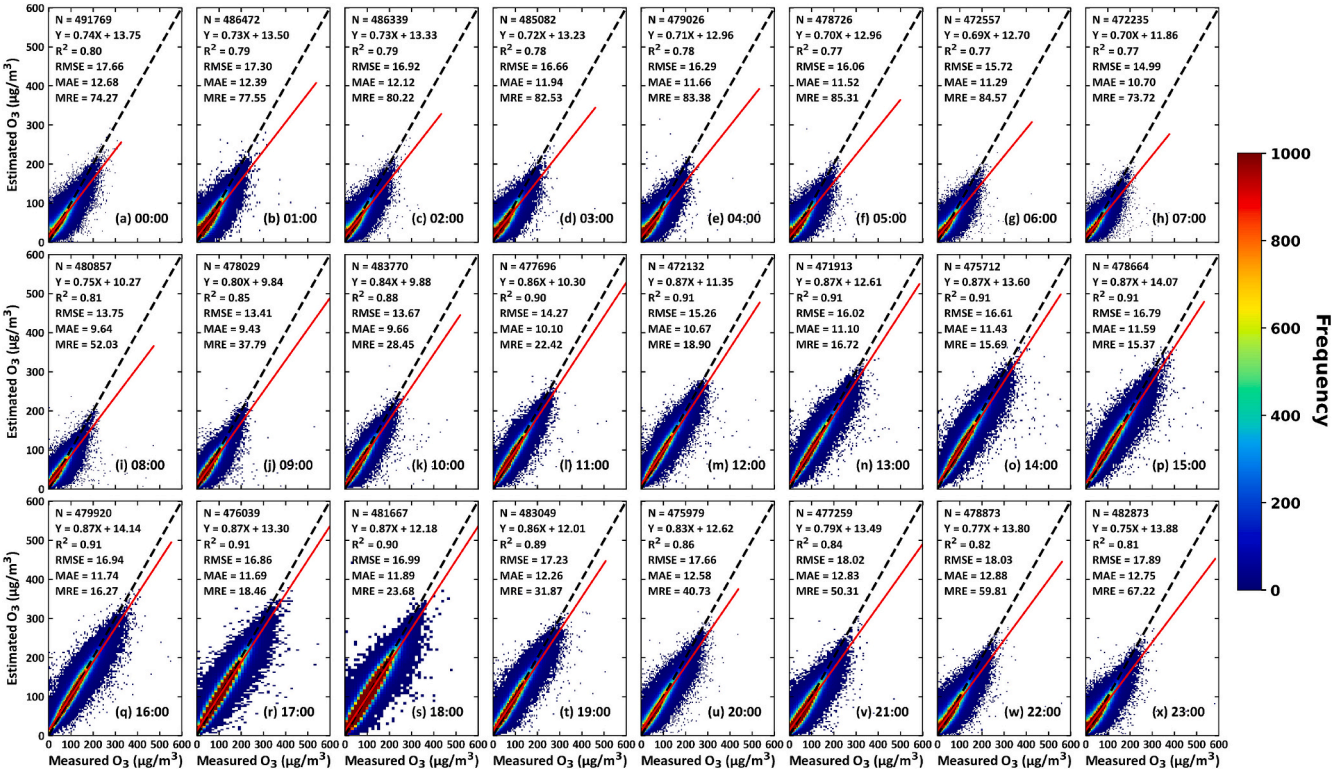


**Fig. 2.** Out-of-sample cross-validation results of hourly $O_3$ estimates (μg/m$^3$) from 00:00 to 23:00 LT for 2019 in China using the 4D-STET model. Black dashed lines denote 1:1 lines, and red solid lines denote best-fit lines from linear regression. The sample size (N), linear-regression relation, coefficient of determination ($R^2$), root-mean-square error (RMSE, μg/m$^3$), mean absolute error (MAE, μg/m$^3$), and mean relative error (MRE, %) are also given. (For interpretation of the references to colour in this figure legend, the reader is referred to the web version of this article.)

less efficiently than tree-based ML models in addressing regression problems (Grinsztajn et al., 2024) because DL is predominantly designed for handling more intricate computer vision tasks (e.g., object recognition and detection), requiring a vast amount of data samples (Shinde and Shah, 2018). Similar comparison results in model accuracy are also obtained from the station-CV and block-CV methods (see Tables S3 and S4) but with a slight decrease compared to the sample-CV results. By comprehensively considering both the model performance and efficiency, the core ET model is thus chosen to estimate surface $O_3$ at the hourly scale in our study. Furthermore, we compared model performance using both traditional and improved spatial and temporal indices. The results indicate that compared with the traditional method (Liu et al., 2020; Wei et al., 2022a), model performance is enhanced, with a 5–6 % reduction in estimated uncertainties (Fig. S2).

#### 3.1.2. Model performance

Figure 2 shows the sample-based overall accuracy of surface $O_3$ estimates at each hour from 0:00 to 23:00 LT using the 4-Dimensional Space-Time Extra-Trees (4D-STET) model. The model accuracy varies for different hours. At 00:00 LT, $O_3$ estimates generally align closely with ground measurements, with a CV-$R^2$ of 0.80 and an RMSE of 17.66 μg/m$^3$. The model performance slightly improves with comparable CV-$R^2$ (0.77–0.79) and lower RMSE values (15–17 μg/m$^3$) until 07:00 LT. During the daytime, the model shows significant improvements, with increasing CV-$R^2$ (slopes closer to 1) and decreasing RMSE values. At 17:00 LT, the performance reaches its peak with a CV-$R^2$ of 0.91, a slope of 0.87, and a RMSE of 16.86 μg/m$^3$. Subsequently, the performance of the model deteriorates gradually. Overall, the model performs well across all hours, with CV-$R^2$ values above 0.77 and RMSE (mean absolute error, MAE) values below 18 (13) μg/m$^3$. Similar trends can be found in the spatial-CV results: The model accuracy of station-CV (block-CV) gradually increases from midnight (0:00 LT) to the afternoon, with increasing CV-$R^2$ and reduced RMSE values, reaching a peak at 17:00 LT, e.g., CV-$R^2$ = 0.90 (0.87) and RMSE = 17.79 (20.08) μg/m$^3$, followed by a gradual decrease thereafter (Figs. S3 and S4).

Overall, on the national scale, the model achieves a high overall (predictive) accuracy in retrieving hourly surface $O_3$ concentrations throughout the day, with average sample (station and block) CV-$R^2$ and RMSE values of 0.89 (0.88 and 0.84) and 16.35 (17.69 and 19.74) μg/m$^3$. The superior performance of the model is also maintained during both daytime (e.g., CV-$R^2$ = 0.92, 0.90 and 0.88, and RMSE = 15.72, 16.72 and 18.75 μg/m$^3$) and nighttime (e.g., CV-$R^2$ = 0.82, 0.78, and 0.73, and RMSE = 16.97, 18.61, and 20.69 μg/m$^3$) (Table 3). The model also performs well in estimating and predicting all-day, daytime, and nighttime hourly surface $O_3$ concentrations at regional scales, especially in the Beijing-Tianjin-Hebei (BTH) region (e.g., sample-CV $R^2$ = 0.87–0.94, station-CV $R^2$ = 0.87–0.94, and block-CV $R^2$ = 0.85–0.93).

Figure 3 shows the model's accuracy of all hourly retrievals in 2019 across China at individual sites. Overall, our model demonstrates strong performance and adaptability in estimating surface hourly $O_3$ levels at most sites without weak spatial patterns. At ~88 % of the sites, sample-based CV-$R^2$ values exceed 0.8, and 76 % (75 %) of the sites have RMSE (MAE) values below 18 (13) μg/m$^3$, particularly in locations within eastern and central China (CV-$R^2$ > 0.9) where the ground observation network is denser (Fig. 3a-c). Spatial patterns for the station-CV and block-CV results are similar, but the model exhibits an overall reduced accuracy in its predictive capability, with decreasing CV-$R^2$ values and increasing uncertainties for most sites across China (Fig. 3d-i). Nevertheless, more than 84 % (74 %), 80 % (63 %), and 74 % (54 %) of the sites still maintain reliability, with high CV-$R^2$ > 0.8, low RMSE < 20 μg/m$^3$, and low MAE < 14 μg/m$^3$ for station-CV (block-CV) results, respectively. Poor performance is primarily located at a few sites in western and northwestern China, as well as some nearby sites like in central China. This variance in the model's predictive ability is mainly caused by large differences in meteorological conditions and pollutant types and the small number of sites in western China. In addition, some input auxiliary variables used for model training, such as BLH and RH, may fail to accurately capture these differences among these sites due to their original coarse resolution (~10 km), resulting in varying levels of accuracy with considerable discrepancies. In general, surface $O_3$ retrievals are highly consistent across national, regional, and site scales, reaffirming the model's robust performance.

### 3.2. Diurnal variations in surface $O_3$ and driving factors

Figures 4 and S5 show satellite-derived gapless and ground-measured surface $O_3$ concentrations at a 1-km resolution for each hour throughout the day in China during the year 2019. In this study, we adopt the China Meteorological Administration's division standards to delineate daytime and nighttime periods, i.e., daytime refers to the 12-h period from 08:00 to 20:00 LT, while the nighttime refers to the 12-h period from 20:00 to 08:00 LT (CMA, 2015). As expected, surface $O_3$ has strong diurnal variations. At 08:00 LT, it is at its lowest level (average = 53.94 ± 10.95 μg/m$^3$), gradually increasing as the sun continues to rise. The increasing rate of surface $O_3$ concentrations is faster in northern China than in southern China, followed by a widespread growing trend in central and eastern China from 10:00 to 12:00 LT. It continues to rise notably over most regions in the domain, with a majority of values surpassing 100 μg/m$^3$, reaching a peak at 15:00 LT (average = 102.56 ± 11.41 μg/m$^3$). After that, areas with high $O_3$ pollution shrink rapidly, with average values dropping from 102.44 ± 11.75 μg/m$^3$ at 16:00 LT to 54.63 ± 12.13 μg/m$^3$ by 07:00 LT the following day. The decreasing rate in southern China outpaces that in northern China, with the fastest decline observed in southeast China.

**Table 3**
Cross-validation (CV) statistics of hourly $O_3$ estimates (μg/m$^3$) for all-day, daytime, and nighttime periods in China and each typical region, using the 4D-STET model. All day represents 00:00–23:00 LT, daytime represents 08:00–20:00 LT, and nighttime represents the other hours.

| Region | Period | Sample-CV | | | Station-CV | | | Block-CV | | |
|---|---|---|---|---|---|---|---|---|---|---|
| | | $R^2$ | RMSE | MAE | $R^2$ | RMSE | MAE | $R^2$ | RMSE | MAE |
| China | All day | 0.89 | 16.35 | 11.53 | 0.88 | 17.69 | 12.46 | 0.84 | 19.74 | 14.27 |
| | Daytime | 0.92 | 15.72 | 10.93 | 0.90 | 16.72 | 11.66 | 0.88 | 18.75 | 13.39 |
| | Nighttime | 0.82 | 16.97 | 12.12 | 0.78 | 18.61 | 13.26 | 0.73 | 20.69 | 15.15 |
| BTH | All day | 0.93 | 17.24 | 11.58 | 0.92 | 17.62 | 11.87 | 0.92 | 18.23 | 12.39 |
| | Daytime | 0.94 | 17.38 | 11.25 | 0.94 | 17.78 | 11.54 | 0.93 | 18.24 | 11.92 |
| | Nighttime | 0.87 | 17.09 | 11.92 | 0.87 | 17.46 | 12.22 | 0.85 | 18.23 | 12.88 |
| YRD | All day | 0.89 | 16.98 | 11.97 | 0.88 | 17.59 | 12.41 | 0.86 | 19.22 | 13.82 |
| | Daytime | 0.91 | 17.36 | 12.12 | 0.90 | 17.85 | 12.46 | 0.88 | 19.44 | 13.83 |
| | Nighttime | 0.81 | 16.58 | 11.83 | 0.79 | 17.33 | 12.36 | 0.75 | 19.00 | 13.81 |
| PRD | All day | 0.89 | 18.50 | 12.76 | 0.87 | 19.97 | 13.78 | 0.83 | 22.45 | 16.01 |
| | Daytime | 0.90 | 19.55 | 13.35 | 0.89 | 20.60 | 14.12 | 0.85 | 23.63 | 16.60 |
| | Nighttime | 0.79 | 17.39 | 12.18 | 0.73 | 19.32 | 13.45 | 0.68 | 21.20 | 15.42 |

BTH: Beijing-Tianjin-Hebei; YRD: Yangtze River Delta; PRD: Pearl River Delta.

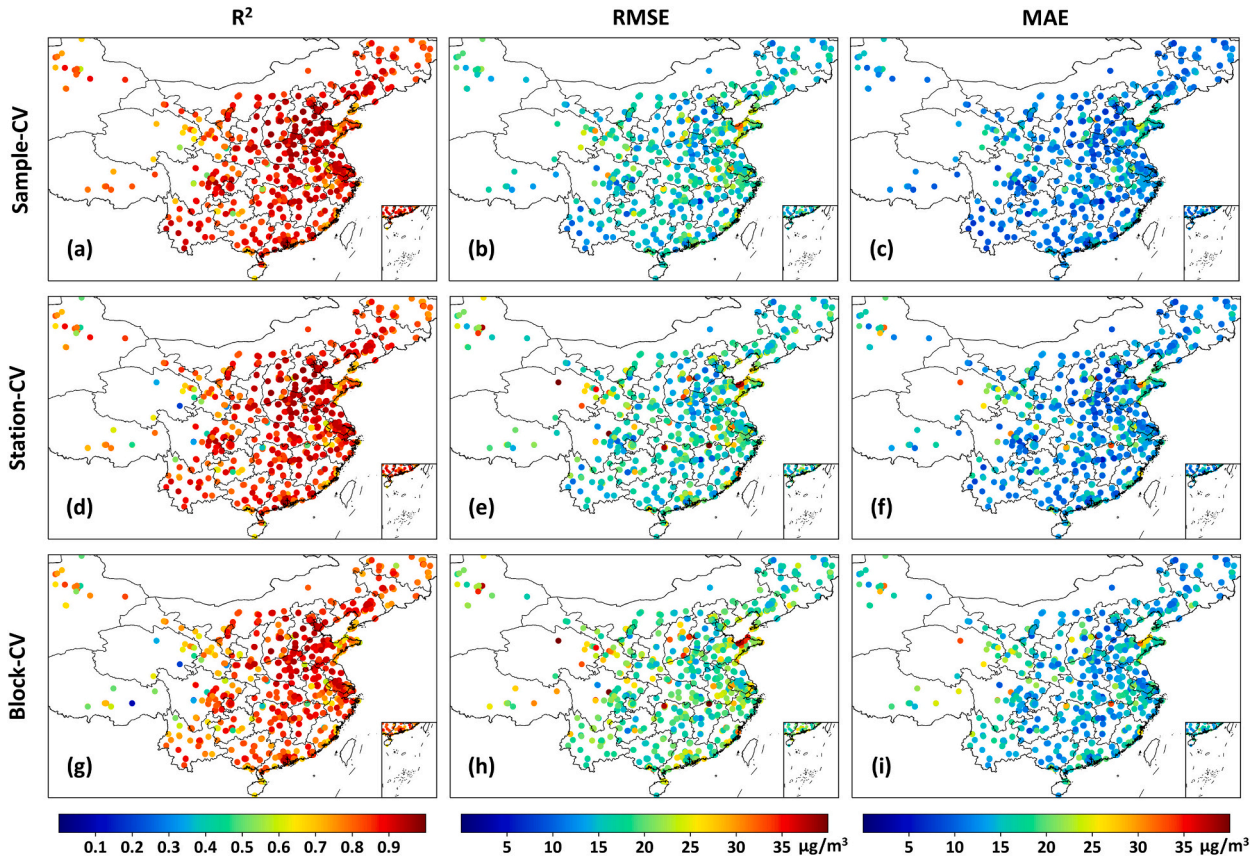


**Fig. 3.** Individual-site-scale (a-c) out-of-sample (top row), (d-f) out-of-station (middle row), and (g-i) out-of-block (bottom row) cross-validation (CV) results for surface $O_3$ retrievals (μg/m$^3$) collected from all hours in 2019 in China using the 4D-STET model.

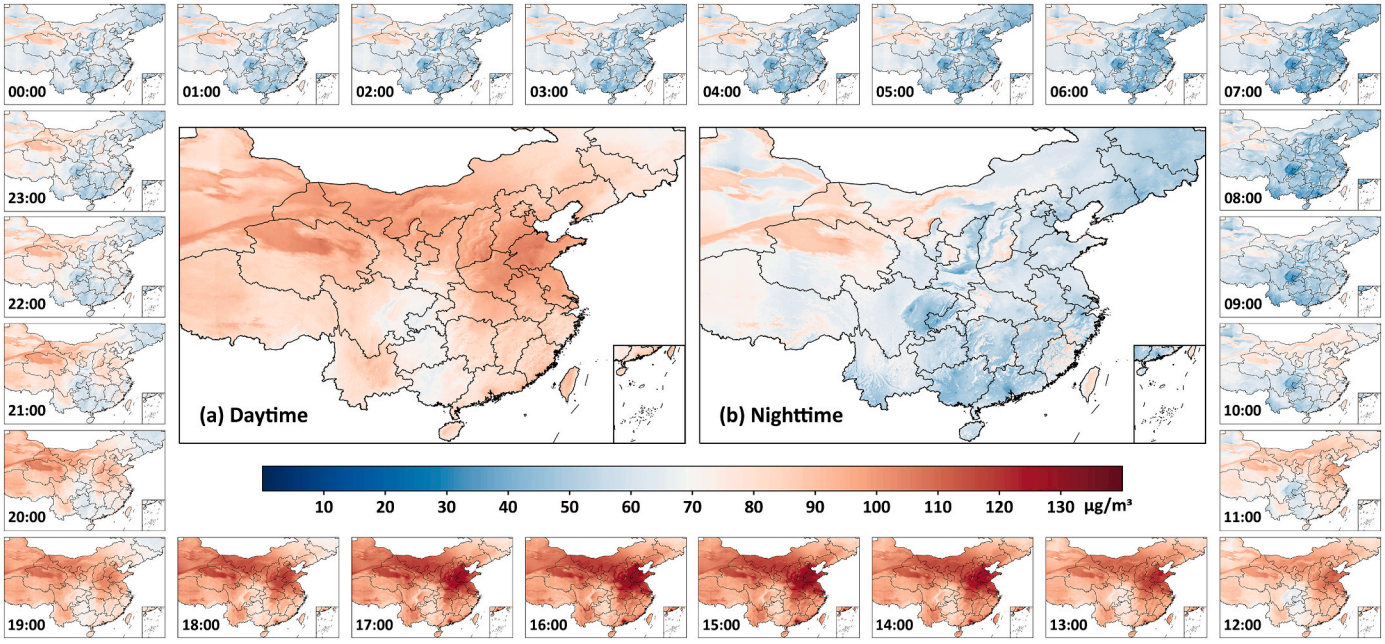


**Fig. 4.** Satellite-derived 1-km-resolution surface $O_3$ concentrations for each hour throughout the day (00:00–23:00 LT, surrounding subplots), along with average maps during the (a) daytime (08:00–20:00 LT) and (b) nighttime (20:00–08:00 LT) in 2019 across China.

During the daytime, surface $O_3$ concentrations in most areas exceed 80 μg/m$^3$, with particularly high levels observed in the North China Plain and northwest China. By contrast, during the nighttime, surface $O_3$ levels consistently fall below 60 μg/m$^3$, except in a few western and central regions. In general, surface $O_3$ concentrations during the daytime (average = 85.88 ± 9.15 μg/m$^3$) are notably higher (~1.4 times) than that at the nighttime (average = 63.78 ± 10.91 μg/m$^3$). This difference is primarily ascribed to the complex interplay of various

atmospheric processes, emissions, and photochemical reactions, e.g., higher oxidant OX ($O_3$ and $NO_2$) levels during the daytime (Han et al., 2011) and lower nighttime BLH facilitating nitric oxide (NO) titration reactions that deplete nighttime $O_3$ (Liao et al., 2023). Similar diurnal variations in surface $O_3$ are observed at regional scales, with the highest values typically occurring around 15:00–16:00 LT (Fig. S6). However, the BTH region seems to show more significant changes, with substantial fluctuations in hourly surface $O_3$ variations. Across different regions, $O_3$ concentrations have relatively consistent diurnal variation patterns throughout all four seasons (Fig. S7). Minimum levels are reached in the early morning (06:00–07:00 LT), gradually increasing thereafter, peaking around 15:00–16:00 LT, and then slowly decreasing. While the general trends are similar across regions, differences exist in the magnitudes of maximum and minimum $O_3$ values (Strode et al., 2019; Xu et al., 2021). In winter, $O_3$ concentrations show minimal diurnal fluctuations, whereas in summer and autumn, the variations are more significant. In general, the diurnal variations in surface $O_3$ concentration from our retrievals are consistent with results obtained from ground-based measurements in China, as well as three typical regions (Figs. 5, and S5-S7).

To gain a deeper insight into the driving factors affecting diurnal variations in surface $O_3$, we utilized XAI technology to compute the SHAP value for each of the variables and investigated their contributions at different hours throughout the day (Fig. 5). In the morning hours (08:00–10:00 LT), the influencing factors are more intricate, with BLH, wind, solar radiation (UV + shortwave), and tropospheric $NO_2$ column ($TNO_2$) emerging as more significant contributors (SHAP = 8–30 %). This can be explained by sunlight elevating solar radiant energy and near-surface temperatures, facilitating the photochemical reaction process (David and Nair, 2011; Han et al., 2011). Additionally, the intermittent vertical turbulent motion associated with BLH and wind transport contributes to a residual $O_3$ layer moving nearer to the surface, consequently elevating surface $O_3$ concentrations (Hu et al., 2012; Morris et al., 2010; Xu et al., 2020). During 11:00–16:00 LT, radiation (14–33 %), LST (11–20 %), RH (8–17 %), and BLH (7–12 %) consistently stand out as the four most influential factors. The primary cause lies in heightened radiation and elevated temperatures substantially stimulating the production of atomic oxygen and oxidants and increasing photochemical reactions (Bloomer et al., 2009; Wei et al., 2022a; Zhang et al., 2023; Zhao et al., 2016). As the day progresses, the contribution of radiation gradually weakens while the roles of temperature and RH undergo significant upswing trends. $TNO_2$ remains a stable and large influence (6 %), primarily driven by continuous human activities and traffic emissions. After solar radiation disappears towards evening, temperature becomes the most critical variable, but its contribution gradually decreases from ~26 % at 19:00 LT to ~3 % at 07:00 LT. In addition, RH also exhibits an overall decreasing trend but still has large impacts (average = 12 %) on surface $O_3$ concentrations, while the contribution of $TNO_2$ exhibits an upward trend, increasing from ~6 % to ~20 % over time. The possible reason is that RH is closely correlated with the dry deposition of $O_3$ and can influence its removal because high RH levels can enhance the $O_3$ deposition rate through the uptake of $O_3$ by water droplets or aerosol particles (Kavassalis and Murphy, 2017). In addition, there are still some chemical reactions in the atmosphere that are related to surface $O_3$, such as those involving HCHO (Stutz et al., 2004) and $NO_x$ (Valuntaitė et al., 2012). Other meteorological (e.g., WS = 13 %) and surface-related (e.g., DEM = 11 % and NDVI = 9 %) factors become increasingly more important in influencing surface $O_3$ variations during nighttime.

In general, during the daytime, over 42 % of the diurnal variation in surface $O_3$ can be attributed to solar radiation (28 %) and surface temperature (14 %). Other meteorological factors contribute ~31 %, with RH (~13 %), BLH (~9 %), and WS (~4 %) having relatively larger influences. However, during the nighttime, $TNO_2$ contributes the most (~16 %), 9 % higher than in the daytime (7 %), followed by LST (13 %). Other meteorological factors comprise ~35 % of the influence, with the three primary variables, i.e., RH, WS, and BLH, contributing at 12 %, 8 %, and 6 %, respectively. In addition, surface-related factors become more important during the nighttime compared to the daytime (13 % versus 10 %). Importantly, our results illustrate the crucial roles of satellite tropospheric $O_3$, $NO_2$, and HCHO, contributing about 3 %, 7 %, and 5 % during the daytime, respectively. Their significance amplifies notably during nighttime, where contributions rise to 27 % versus 15 %, particularly pronounced for $NO_2$ (~16 %). The reason is that during

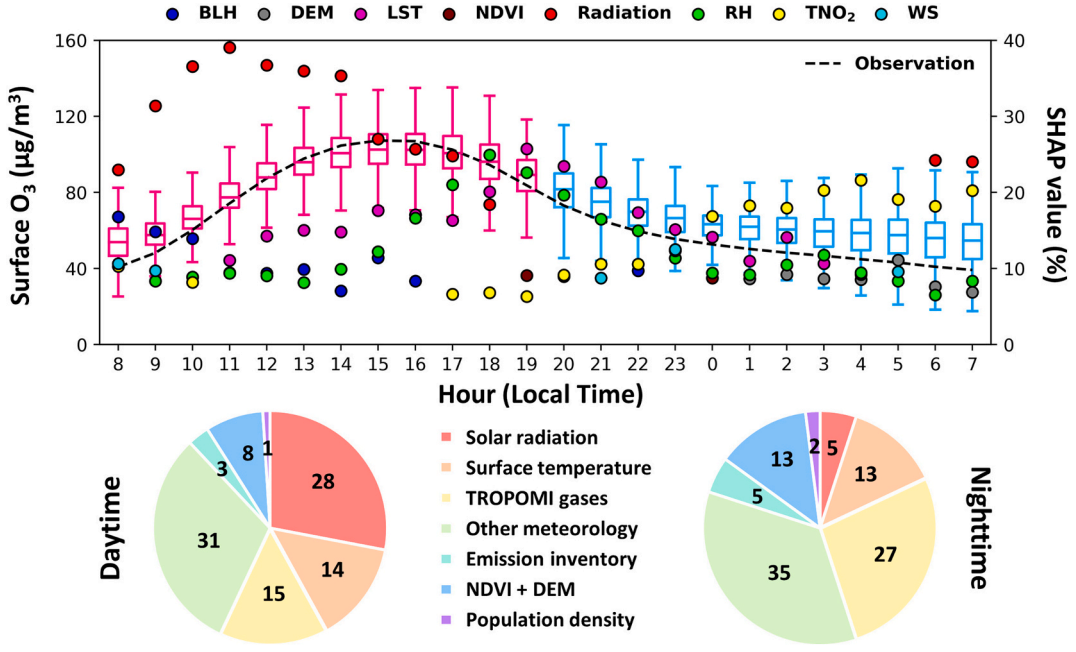


**Fig. 5.** Time series of hourly surface $O_3$ variations (boxplots) and top-four driving factors (colored dots) throughout the day in 2019 in China. The black dashed line represents the diurnal variation observed from ground measurements. The two pie charts illustrate the contributions of driving-factor categories during the daytime (08:00–20:00 LT) and nighttime (20:00–08:00 LT). Solar radiation includes DSR, UVA, and UVB. Other meteorological variables include BLH, RH, TP, SP, WD, and WS. TROPOMI gases include $TO_3$, $TNO_2$, and THCHO. The emission inventory includes $NO_x$, VOCs, and CO.

nighttime, the NO titration effect consumes nocturnal $O_3$, consequently elevating $NO_2$ concentrations ($NO + O_3 \rightarrow NO_2 + O_2$), thereby further depleting $O_3$ to produce $NO_3$ ($NO_2 + O_3 \rightarrow NO_3 + O_2$) (He et al., 2018; Li et al., 2023a). However, tropospheric $O_3$ is generally less important than the other two gases, perhaps due to the larger uncertainties encountered during the conversion process from total column amount to tropospheric column amount using $O_3$ profile data. Nevertheless, differences exist at the regional scale (Fig. S6). In the BTH and Yangtze River Delta (YRD) regions, LST (37 % and 32 %) and radiation (25 % and 16 %) contribute the most during the daytime, while RH, wind, TP, and SP are more important meteorological factors during the nighttime. $TNO_2$ remains relatively impactful (11 % and 9 %) throughout the day. By contrast, in the Pearl River Delta (PRD) region, RH contributes the most during the daytime and nighttime (23 % and 18 %, respectively), and meteorological factors contribute more significantly to surface $O_3$ variations compared to other regions. This region is closer to the sea, with southwest and southeast monsoons prevailing in the summer, and is affected by more weather systems (e.g., southwesterly wind, typhoons, and weak cyclones) (Han et al., 2020; Jiang et al., 2015).

### 3.3. MDA8 $O_3$ levels and exposure risk

Using 24-hourly data, we first calculate MDA8 $O_3$ concentrations across China and evaluate the population risk exposure to short-term $O_3$ pollution using World Health Organization (WHO) air quality standards updated in 2021 (WHO, 2021) (Fig. 6). MDA8 $O_3$ concentrations mostly fall within the range of 81 to 115 μg/m$^3$ (95th percentile), with a population-weighted average of 101.7 μg/m$^3$ in 2019 (Fig. 6a). Serious pollution situations are mainly distributed in the North China Plain (especially in major parts of Shandong, Hebei, and Henan provinces: MDA8 $O_3$ > 120 μg/m$^3$) and north-central regions. By contrast, the remaining areas generally experience low levels, especially in northeast and southwest China (MDA8 $O_3$ < 90 μg/m$^3$). Concerning the daily population risk of $O_3$ exposure, we found that ~43 % (61 %) of all (populated) areas in China encounter severe $O_3$ pollution, with at least one day surpassing the WHO's recommended short-term interim target 1 (i.e., daily MDA8 $O_3$ = 160 μg/m$^3$). However, the exposure risk is usually low (less than 20 % of days) in most regions (Fig. 6b). Regarding the short-term interim target 2 (i.e., daily MDA8 $O_3$ = 120 μg/m$^3$), areas exposed to a one-day risk expand significantly, reaching 97 % in all areas and 98 % in populated areas. The frequency also increases rapidly, with some eastern areas experiencing pollution for up to half of the year (Fig. 6c). Most notably, when looking at the expected short-term air quality guidance (AQG) level (i.e., daily MDA8 $O_3$ = 100 μg/m$^3$), 100 % of areas and the entire population are exposed to unhealthy air for at least one day, with a substantial risk intensity ranging from 20 % to 90 % across the domain (Fig. 6d). These findings signify a serious risk of short-term $O_3$ exposure, underscoring the urgent requirement for

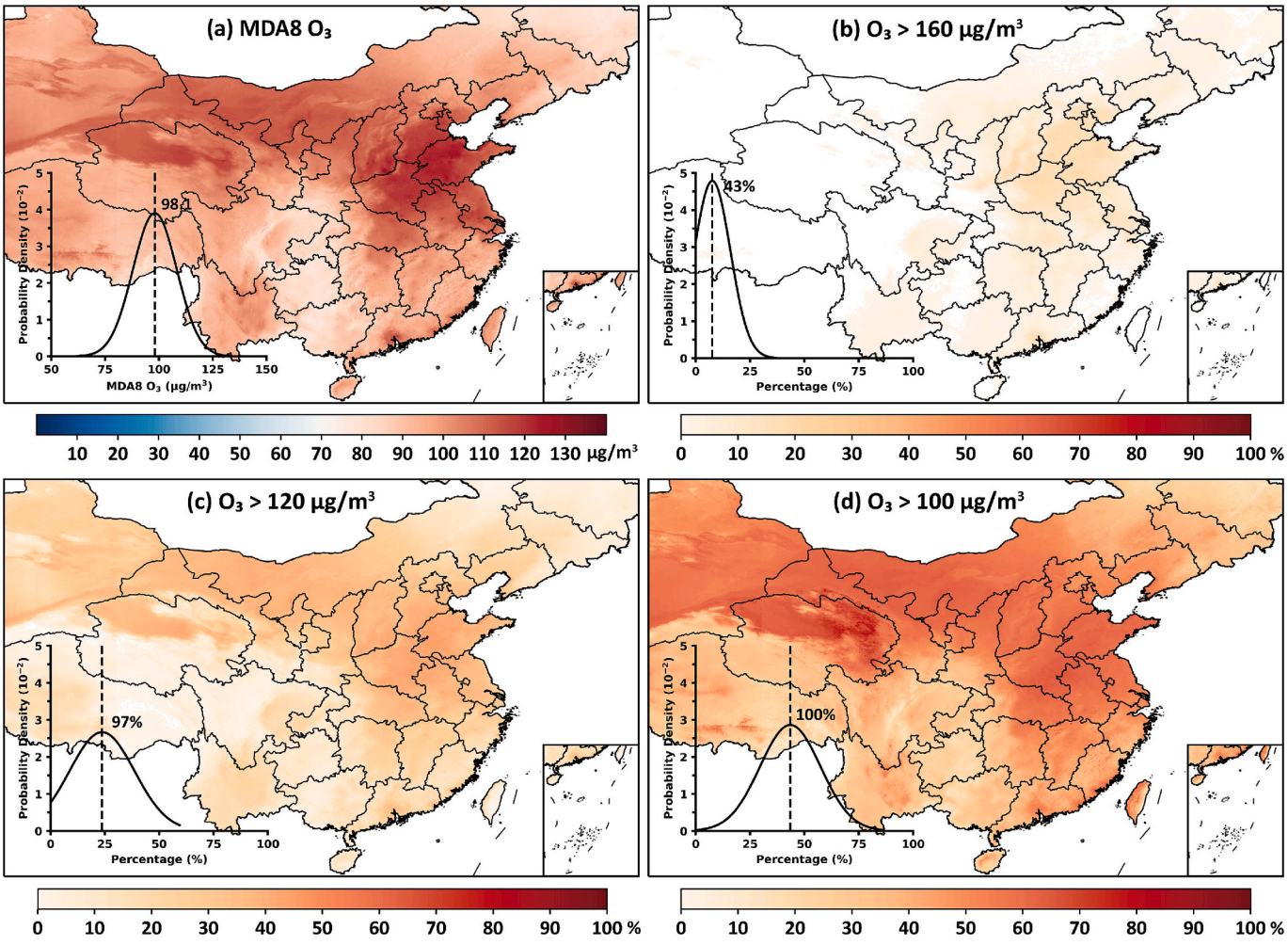


**Fig. 6.** Spatial distributions of (a) MDA8 $O_3$ concentration (μg/m$^3$) and the percentage (%) of days exceeding the WHO-recommended short-term (b) interim target 1 (daily MDA8 $O_3$ = 160 μg/m$^3$), (c) interim target 2 (daily MDA8 $O_3$ = 120 μg/m$^3$), and (d) air quality guideline level (daily MDA8 $O_3$ = 100 μg/m$^3$) for 2019 in China. The inserted lower-left plots show probability density curves. The number in (a) is the annual average of MDA8 $O_3$ in China, and the numbers in (b-d) indicate the percentages of pollution days for all regions, respectively.

environmental protection measures to control surface $O_3$ pollution, improve air quality, and promote future health benefits, especially in densely populated regions.

### 3.4. Surface $O_3$ phytotoxicity indices and impacts

Figure 7 illustrates the spatial distribution of six main surface $O_3$ phytotoxicity indices calculated from 24-hourly data in China for the year 2019. Specifically, M7 and M12 have similar spatial patterns, ranging between 32 to 45 ppb and 33 to 47 ppb (95th percentile), with an average of 39.3 and 40.1 ppb, respectively. Elevated values are predominantly concentrated in the western regions of Shandong province and scattered areas in northern China (Fig. 7a-b). Conversely, most other areas maintain low levels, especially in western, southwest, and northeastern China (M7 and M12 < 35 ppb). There is a substantial disparity between AOT0 and AOT40, where the former ranges from 52 to 84 ppm (95th percentile), with an average of 66.9 ppm, and the latter is mostly within the 6–32 ppm range (average = 15.9 ppm). This distinction is attributed to AOT40 incorporating a threshold for hourly $O_3$ accumulation, while there is no criterion for AOT0. Nevertheless, extremely high AOT0 values are present in the North China Plain (particularly in Shandong and Tianjin), as well as in the western and central regions of Inner Mongolia and certain areas in northeastern China like Liaoning (Fig. 7c). Similar spatial patterns are observed for AOT40, albeit with significantly lower levels. Note that ~95 %, 98 %, and 100 % of vegetated areas in China exceed the defined critical levels of AOT40 at 6 ppm, 5 ppm, and 3 ppm, respectively. The spatial patterns of SUM06 (ranging from 0.12 to 54, average = 21.9 ppm) and W126 (ranging from 4 to 44, average = 16.9 ppm) are generally in close alignment with that of AOT40 but with higher levels in the North China Plain (Fig. 7e-f). However, about 55 %, 65 %, and 70 % of vegetated areas in China surpass the SUM06 critical levels of 15 ppm, 10 ppm, and 8 ppm, respectively. Furthermore, ~23 % and 82 % of vegetated areas in China are above the W126 critical levels of 23.8 ppm and 5.9 ppm, respectively. In general, the majority of vegetated areas in China in 2019 experienced surface $O_3$ phytotoxicity, with the North China Plain being the most severely impacted region.

We also quantitatively investigated the influence of surface $O_3$ pollution on various types of vegetation (Fig. 8), observing predominantly negative correlations between six $O_3$ phytotoxicity indices and four vegetation abundance indices. It is clear that vegetation growth and development are susceptible to exposure to surface $O_3$ pollution through phytotoxicity, with the extent of damage depending on the plant species, as implied by the varying strengths of the correlations. For croplands, AOT0, AOT40, and SUM06 are more associated with various vegetation abundance indices, particularly GPP, with $R$ values of −0.43 ($p < 0.001$), −0.41 ($p < 0.001$), and −0.41 ($p < 0.001$), respectively. Forests also have stronger responses to $O_3$ pollution, showing heightened sensitivities, especially with AOT0 ($R = -0.35$ to $-0.53$, $p < 0.001$), AOT40 ($R = -0.21$ to $-0.45$, $p < 0.001$), and W126 ($R = -0.15$ to $-0.29$, $p < 0.001$). For grasslands, the correlations between phytotoxicity indices and abundance indices continuously strengthen, particularly with AOT0 ($R = -0.42$ to $-0.59$, $p < 0.001$), M12 ($R = -0.42$ to $-0.58$, $p < 0.001$), and M7 ($R = -0.34$ to $-0.54$, $p < 0.001$). Among all types of vegetation, AOT0 exhibits the most pronounced response to variations in vegetation growth, displaying the highest correlations with various abundance indices ($R = -0.19$ to $-0.59$, $p < 0.001$), followed by M12 ($R = -0.11$ to $-0.58$, $p < 0.001$), and M7 ($R = -0.11$ to $-0.54$, $p < 0.001$). In general, GPP has the strongest sensitivity to surface $O_3$ exposure, particularly in conjunction with AOT0, with the strongest correlation across all vegetated areas ($R = -0.53$, $p < 0.001$), as well as in croplands ($R = -0.43$, $p < 0.001$), forests ($R = -0.46$, $p < 0.001$), and grasslands ($R = -0.59$, $p < 0.001$), consistent with findings from a previous study (Zhu et al., 2022). This is further supported by its consistently strongest correlations with other $O_3$-exposure phytotoxicity indices. This can be attributed to ambient $O_3$'s ability to enter leaves through stomata, causing damage to biological macromolecules and cell death (Kangasjarvi et al., 2005). This, in turn, reduces leaf stomatal conductance and photosynthetic rates (Ainsworth et al., 2012), ultimately leading to declines in primary metabolism, leaf area, biomass, and further reductions in GPP (Jin et al., 2023; Proietti et al., 2016).

### 3.5. Comparison with related studies

Last, we compared our results with related research focusing on surface $O_3$ retrievals across China (Table 4). Most previous studies were

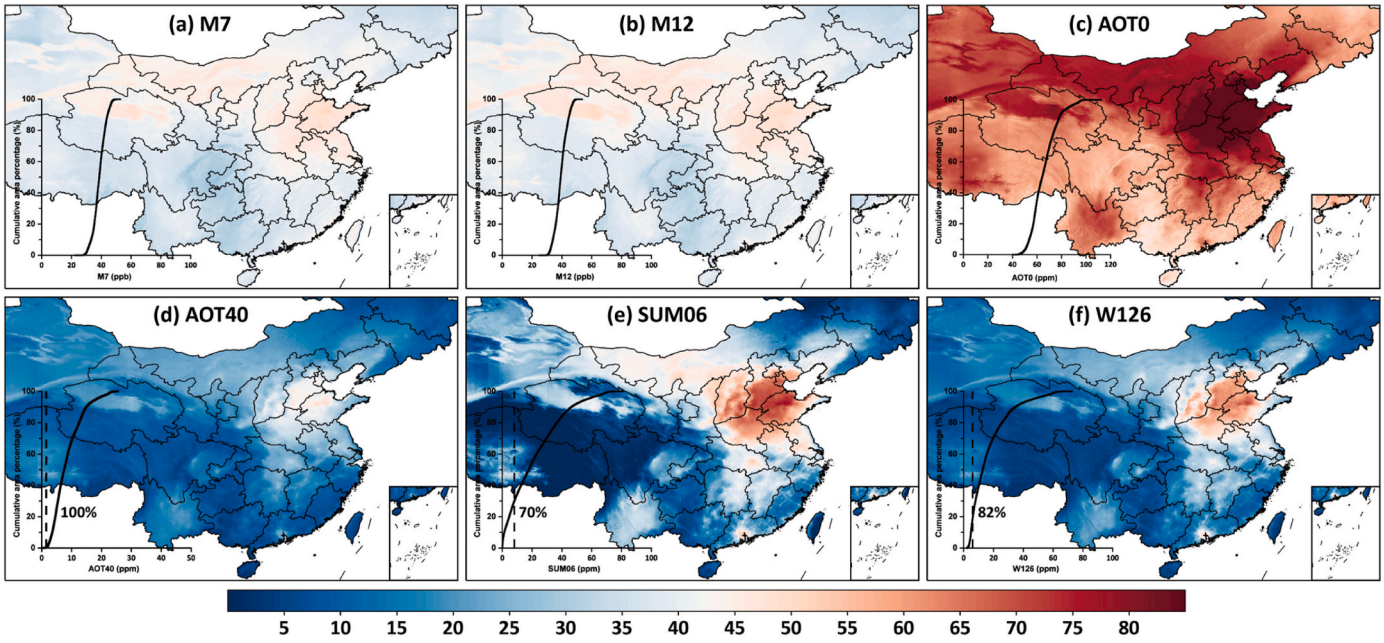


**Fig. 7.** Spatial distributions of estimated (a) M7 (ppb), (b) M12 (ppb), (c) AOT0 (ppm), (d) AOT40 (ppm), (e) SUM06 (ppm), and (f) W126 (ppm) across China in 2019. The inserted lower-left plots show cumulative area percentages for vegetated areas in China. The black dotted lines in (d-f) show the lowest critical levels (i.e., 3, 8, and 5.9 ppm, respectively). The numbers in (d-f) indicate cumulative percentages exceeding the specific critical level.

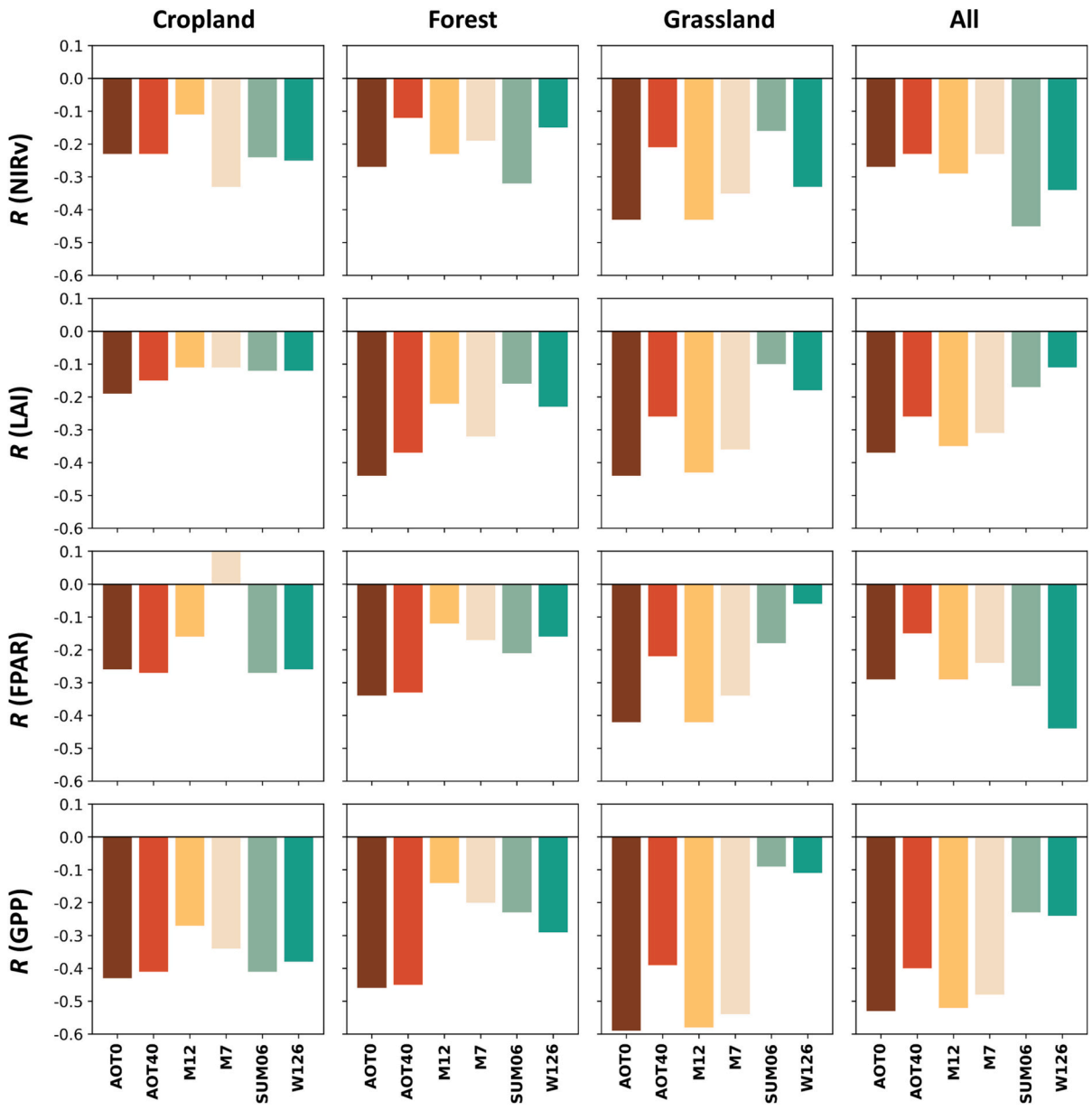


**Fig. 8.** Correlation analysis between vegetation abundance indices (i.e., NIRv, LAI, FPAR, and GPP) and $O_3$-exposure phytotoxicity indices (i.e., AOT0, AOT40, M12, M7, SUM06, and W126) for various vegetated types, i.e., all vegetated areas (sample size, $N = 9{,}109{,}181$), forest ($N = 1{,}746{,}937$), grassland ($N = 5{,}281{,}879$), and cropland ($N = 2{,}080{,}365$) in China in 2019. All correlations are statistically significant at the 99.9 % ($p < 0.001$) confidence level.

**Table 4**
Model performance comparison in estimating hourly surface $O_3$ concentrations in China from previous studies.

| Model | Duration | Spatial resolution | Overall accuracy | | | Missing values | Literature |
|---|---|---|---|---|---|---|---|
| | | | CV-$R^2$ | RMSE | MAE | | |
| LSTM | All day (00:00–23:00 LT) | 10 km | 0.72 | 22.98 | – | No | Zhang et al. (2024) |
| DF | All day (00:00–23:00 LT) | 10 km | 0.80 | 18.56 | 13.60 | No | Zhu et al. (2023) |
| BT | Daytime (09:00–16:00 LT) | 5 km | 0.87 | 18.30 | 13.30 | No | Zhang et al. (2023) |
| DF | Daytime (10:00–15:00 LT) | 5 km | 0.91 | 12.74 | 8.25 | Yes | Chen et al. (2023b) |
| SGLboost | Daytime (09:00–18:00 LT) | 2 km | 0.85 | 19.04 | – | Yes | Wang et al. (2022c) |
| 4D-STET | Daytime (09:00–16:00 LT) | 1 km | 0.92 | 15.43 | 10.71 | No | This study |
| | Daytime (10:00–15:00 LT) | | 0.91 | 15.48 | 10.78 | | |
| | Daytime (09:00–18:00 LT) | | 0.92 | 15.74 | 10.93 | | |
| | Daytime (08:00–20:00 LT) | | 0.92 | 15.72 | 10.93 | | |
| | Nighttime (20:00–08:00 LT) | | 0.82 | 16.97 | 12.12 | | |
| | All day (00:00–23:00 LT) | | 0.89 | 16.35 | 11.53 | | |

LSTM: Long Short-Term Memory; DF: Deep Forest; BT: Bagged-Tree; SGLboost: Self-adaptive Geospatially Local categorical boosting; 4D-STET: 4-Dimensional Space-Time Extra-Trees.

concerned with the daily level, using MDA8 $O_3$ measurements calculated from hourly data as the baseline for model training (Liu et al., 2020; Song et al., 2022; Wei et al., 2022a; Xue et al., 2020). In fact, MDA8 is not a straightforward multi-hour average but an iterative daily maximum 8-h average, which can lead to substantial deviations in modeling interpolated results, particularly in remote areas lacking measurements. Accurate MDA8 calculations require 24-h of retrievals, but few studies have addressed this issue (Chen et al., 2023b; Wang et al., 2022c; Xue et al., 2022; Zhang et al., 2023). All of these studies have also exclusively focused on retrieving daytime surface $O_3$ concentrations, with durations (< 10 h) falling significantly short of the requirements to calculate air quality and $O_3$-exposure phytotoxicity indices. In addition, their retrieved hourly surface $O_3$ concentrations often have sparse spatial resolutions (2–10 km), significantly constraining their applicability in small-scale areas such as urban environments. This is evidenced by the strong $O_3$ heterogeneity observed when analyzing surface $O_3$ differences at multiple closely located sites in typical regions across China (Text S1, and Figs. S8 and S9). Furthermore, previous estimates suffer from severe spatial discontinuities due to large gaps of missing values in critical satellite optical input variables (e.g., Himawari-8 top-of-the-atmosphere radiation and brightness temperatures) caused by cloud contaminations (Chen et al., 2023b; Wang et al., 2022c). Importantly, our model exhibits superior overall accuracy compared to the performance of AI models in previous studies using data from the same period, including LSTM (e.g., CV-$R^2$ = 0.72; Zhang et al., 2024), BT (e.g., CV-$R^2$ = 0.87; Zhang et al., 2023), DF (e.g., CV-$R^2$ = 0.91 and 0.80; Chen et al., 2023b; Zhu et al., 2023), and SGLboost (e.g., CV-$R^2$ = 0.85, Wang et al., 2022c). The improvements result from the use of a more competent ML model and more variables affecting $O_3$, such as satellite tropospheric $NO_2$ and HCHO, along with major $O_3$ precursors. This approach allows for a more comprehensive capture of the impact of photochemical reactions on surface $O_3$ generation. Additionally, we address the obvious heterogeneities of surface $O_3$ by incorporating novel spatiotemporal information during the modeling process. Our study presents unique information by first offering a spatially (100 % coverage) continuous dataset of 24-hourly surface $O_3$ concentrations across China, encompassing the full temporal range (0:00–23:00 LT) at a high spatial resolution of 1 km.

### 3.6. Summary and conclusions

Surface $O_3$ is a critical atmospheric pollutant gas influencing air quality, posing a major human health risk, as well as plant well-being risk. To overcome limitations encountered in previous studies, e.g., low temporal resolution (mostly daily, with only a few hourly observations during the daytime), sparse spatial resolution, and substantial spatial gaps in data retrievals, we refined a total of 15 AI models by introducing multidimensional spatiotemporal information to enhance their capabilities. The best-performing model (i.e., the 4D-STET model) was then selected to derive for the first time gapless surface $O_3$ concentrations in China at 24-hourly temporal and 1-km spatial resolutions from the geostationary-satellite-derived solar radiation and surface tempuratureproducts and many other ancillary data for the year 2019. Cross-validations demonstrate the robustness of our model in capturing the diurnal variations of surface $O_3$ concentrations, with overall sample-based (station-based and block-based) CV-$R^2$ values of 0.89 (0.88 and 0.84), 0.92 (0.90 and 0.88), and 0.82 (0.78 and 0.73), with corresponding RMSE values of 16.35 (17.69 and 19.74) μg/m$^3$, 15.72 (16.72 and 18.75) μg/m$^3$, and 16.97 (18.61 and 20.69) μg/m$^3$ during all times (00:00–23:00 LT), daytime (08:00–20:00 LT), and nighttime (20:00–08:00 LT), respectively. The availability of temporally continuous surface $O_3$ data facilitates our capacity to analyze diurnal variations, daily exposure risks, and phytotoxicity impacts at different spatiotemporal scales throughout China.

Surface $O_3$ levels showed strong diurnal variations, steadily rising from sunrise, peaking around 15:00 LT, and continuously decreasing thereafter. XAI-SHAP analysis results revealed that shortwave and UV radiation, along with LST, explain about 42 % of the surface $O_3$ variations during the daytime, while tropospheric $NO_2$ plays the most significant role during the nighttime, contributing approximately 16 %. In 2019, approximately 61 % (43 %), 98 % (97 %), and 100 % (100 %) of populated areas (entire areas) faced short-term surface $O_3$ exposure risk for at least one day, with daily MDA8 $O_3$ surpassing the WHO's air quality standards of 160 μg/m$^3$, 120 μg/m$^3$, and 100 μg/m$^3$, respectively. Furthermore, ~100 %, 98 %, and 95 % of vegetated areas in China exceeded the critical levels of AOT40 at 3 ppm, 5 ppm, and 6 ppm, respectively. For SUM06, ~70 %, 65 %, and 55 % of vegetated areas surpassed the critical levels of 8 ppm, 10 ppm, and 15 ppm, respectively. As for W126, ~82 % and 23 % of vegetated areas exceeded the critical levels of W126 at 5.9 ppm and 23.8 ppm, respectively. These findings highlight the urgent need for environmental protection measures to mitigate surface $O_3$ pollution and promote the health of both the public and vegetation in the future. Despite the consistent negative correlations, GPP demonstrates the strongest response to surface $O_3$ pollution among all vegetation (ozone-exposure) phytotoxicity indices, encompassing various vegetated types, especially when combined with AOT0 ($R = -0.43$ to $-0.59$, $p < 0.001$). In a future study, we will explore more powerful AI methods with improved capabilities in handling time-series data, such as Transformer (Vaswani et al., 2017; Wei et al., 2024), and integrate relevant gas data from GEO satellites such as GEMS and TEMPO to further refine the estimation of hourly surface $O_3$ concentrations. We also intend to apply our methodology to generate a long-term hourly surface $O_3$ dataset to provide more detailed insights into air quality and phytotoxic damage caused by surface $O_3$ pollution.

## CRediT authorship contribution statement

**Fan Cheng:** Writing – original draft, Validation, Software, Methodology, Formal analysis, Data curation. **Zhanqing Li:** Writing – review & editing, Supervision, Methodology, Funding acquisition. **Zeyu Yang:** Data curation. **Ruohan Li:** Data curation. **Dongdong Wang:** Writing – review & editing, Data curation. **Aolin Jia:** Data curation. **Ke Li:** Writing – review & editing. **Bin Zhao:** Writing – review & editing, Data curation. **Shuxiao Wang:** Writing – review & editing, Data curation. **Dejia Yin:** Data curation. **Shengyue Li:** Data curation. **Wenhao Xue:** Funding acquisition, Data curation. **Maureen Cribb:** Writing – review & editing. **Jing Wei:** Writing – review & editing, Supervision, Methodology.

## Declaration of competing interest

The authors declare that they have no conflict of interest.

## Data availability

Chinese $O_3$ measurements are available at http://www.cnemc.cn. The Himawari-8 Downward Shortwave Radiation and Photosynthetically Available Radiation products are available at https://data.nas.nasa.gov/geonex/geonexdata/HIMAWARI8/GEONEX-L2/DSR-PAR/ and https://www.eorc.jaxa.jp/ptree/. The GHA Land Surface Temperature product is available at http://glass.umd.edu/allsky_LST/GHA-LST/2019/. The TROPOMI tropospheric $O_3$, $NO_2$, and HCHO columns products are available at https://browser.dataspace.copernicus.eu/. The ERA5 reanalysis is available at https://cds.climate.copernicus.eu/. The CAMS global reanalysis is available at https://ads.atmosphere.copernicus.eu/. The ABaCAS-EI v2.0 emission inventory is available at doi:10.6084/m9.figshare.21777005.v1. The SRTM DEM data is available at https://www2.jpl.nasa.gov/srtm/. LandScan™ population data is available at https://landscan.ornl.gov/. The MODIS series products, including NDVI (MOD13A2), nadir reflectance (MCD43A4), LAI and FPAR (MOD15A2H), and Land Cover Type (MCD12Q1) products are available at https://www.earthdata.nasa.gov/. GPP data is available at http://www.nesdc.org.cn/sdo/detail?

id=612f42ee7e28172cbed3d809. The generated 24-hourly 1-km surface $O_3$ datasets and codes can be found at doi:10.5281/zenodo.10035857.

## Acknowledgments

This work was supported by the National Natural Science Foundation of China (42030606 and 42207541), as well as the Samsung Advanced Institute of Technology.

## Appendix A. Supplementary data

Supplementary data to this article can be found online at https://doi.org/10.1016/j.rse.2024.114482.

## References

Ainsworth, E.A., Yendrek, C.R., Sitch, S., Collins, W.J., Emberson, L.D., 2012. The effects of tropospheric ozone on net primary productivity and implications for climate change. Annu. Rev. Plant Biol. 63, 637–661. https://doi.org/10.1146/annurev-arplant-042110-103829.

Allen, R.J., Sherwood, S.C., Norris, J.R., Zender, C.S., 2012. Recent northern hemisphere tropical expansion primarily driven by black carbon and tropospheric ozone. Nature 485, 350–354. https://doi.org/10.1038/nature11097.

Badgley, G., Field, C.B., Berry, J.A., 2017. Canopy near-infrared reflectance and terrestrial photosynthesis. Sci. Adv. 3, e1602244. https://doi.org/10.1126/sciadv.1602244.

Barnard, W.F., Saxena, V.K., Wenny, B.N., DeLuisi, J.J., 2003. Daily surface UV exposure and its relationship to surface pollutant measurements. J. Air Waste Manage. Assoc. 53, 237–245. https://doi.org/10.1080/10473289.2003.10466134.

Bloomer, B.J., Stehr, J.W., Piety, C.A., Salawitch, R.J., Dickerson, R.R., 2009. Observed relationships of ozone air pollution with temperature and emissions. Geophys. Res. Lett. 36. https://doi.org/10.1029/2009GL037308.

Brauer, M., Freedman, G., Frostad, J., van Donkelaar, A., Martin, R.V., Dentener, F., van Dingenen, R., Estep, K., Amini, H., Apte, J.S., Balakrishnan, K., Barregard, L., Broday, D., Feigin, V., Ghosh, S., Hopke, P.K., Knibbs, L.D., Kokubo, Y., Liu, Y., Ma, S., Morawska, L., Sangrador, J.L.T., Shaddick, G., Anderson, H.R., Vos, T., Forouzanfar, M.H., Burnett, R.T., Cohen, A., 2016. Ambient air pollution exposure estimation for the global burden of disease 2013. Environ. Sci. Technol. 50, 79–88. https://doi.org/10.1021/acs.est.5b03709.

Breiman, L., 2001. Random forests. Mach. Learn. 45, 5–32. https://doi.org/10.1023/A:1010933404324.

Cai, M., Wei, J., Zhang, S., Liu, W., Wang, L., Qian, Z., Lin, H., Liu, E., McMillin, S.E., Cao, Y., Yin, P., 2023. Short-term air pollution exposure associated with death from kidney diseases: a nationwide time-stratified case-crossover study in China from 2015 to 2019. BMC Med. 21, 32. https://doi.org/10.1186/s12916-023-02734-9.

Capilla, C., 2016. Prediction of hourly ozone concentrations with multiple regression and multilayer perceptron models. Int. J. SDP 11, 558–565. https://doi.org/10.2495/SDP-V11-N4-558-565.

Chen, B., Wang, Y., Huang, J., Zhao, L., Chen, R., Song, Z., Hu, J., 2023b. Estimation of near-surface ozone concentration and analysis of main weather situation in China based on machine learning model and Himawari-8 TOAR data. Sci. Total Environ. 864, 160928. https://doi.org/10.1016/j.scitotenv.2022.160928.

Chen, C., Li, T., Sun, Q., Shi, W., He, M.Z., Wang, J., Liu, J., Zhang, M., Jiang, Q., Wang, M., Shi, X., 2023a. Short-term exposure to ozone and cause-specific mortality risks and thresholds in China: evidence from nationally representative data, 2013-2018. Environ. Int. 171, 107666. https://doi.org/10.1016/j.envint.2022.107666.

Chen, J., Shen, H., Li, X., Li, T., Wei, Y., 2022a. Ground-level ozone estimation based on geo-intelligent machine learning by fusing in-situ observations, remote sensing data, and model simulation data. Int. J. Appl. Earth Obs. Geoinf. 112, 102955. https://doi.org/10.1016/j.jag.2022.102955.

Chen, T., Guestrin, C., 2016. XGBoost: a scalable tree boosting system. In: Proceedings of the 22nd ACM SIGKDD International Conference on Knowledge Discovery and Data Mining, pp. 785–794. https://doi.org/10.1145/2939672.2939785.

Chen, Y., Zhou, Y., Nixia Ciren, Zhang H., Wang, C., Deji, Gesang, Wang, X., 2022b. Spatiotemporal variations of surface ozone and its influencing factors across Tibet: a Geodetector-based study. Sci. Total Environ. 813, 152651. https://doi.org/10.1016/j.scitotenv.2021.152651.

China Meteorological Administration (CMA), 2015. What Part of the Time Does "Day" and "Night" Refer To? (accessed 25 March, 2024). https://www.cma.gov.cn/wmhd/gzly/cjwt/.

David, L.M., Nair, P.R., 2011. Diurnal and seasonal variability of surface ozone and $NO_x$ at a tropical coastal site: association with mesoscale and synoptic meteorological conditions. J. Geophys. Res. 116, D10303. https://doi.org/10.1029/2010JD015076.

Di, Q., Rowland, S., Koutrakis, P., Schwartz, J., 2017. A hybrid model for spatially and temporally resolved ozone exposures in the continental United States. J. Air Waste Manage. Assoc. 67 (1), 39–52. https://doi.org/10.1080/10962247.2016.1200159.

Du, K., Leung, C., Mow, W., Swamy, M., 2022. Perceptron: learning, generalization, model selection, fault tolerance, and role in the deep learning era. Mathematics 10. https://doi.org/10.3390/math10244730.

Fares, S., Vargas, R., Detto, M., Goldstein, A.H., Karlik, J., Paoletti, E., Vitale, M., 2013. Tropospheric ozone reduces carbon assimilation in trees: estimates from analysis of continuous flux measurements. Global Change Bio. 19, 2427–2443. https://doi.org/10.1111/gcb.12222.

Freund, Y., Schapire, R.E., 1997. A decision-theoretic generalization of on-line learning and an spplication to boosting. J. Comput. Syst. Sci. 55, 119–139. https://doi.org/10.1006/jcss.1997.1504.

Friedman, J.H., 2001. Greedy function approximation: a gradient boosting machine. Ann. Stat. 29. https://doi.org/10.1214/aos/1013203451.

Fu, T.-M., Tian, H., 2019. Climate change penalty to ozone air quality: review of current understandings and knowledge gaps. Curr. Pollut. Rep. 5, 159–171. https://doi.org/10.1007/s40726-019-00115-6.

Fuhrer, J., Skärby, L., Ashmore, M.R., 1997. Critical levels for ozone effects on vegetation in Europe. Environ. Pollut. 97, 91–106. https://doi.org/10.1016/S0269-7491(97)00067-5.

Geurts, P., Ernst, D., Wehenkel, L., 2006. Extremely randomized trees. Mach. Learn. 63, 3–42. https://doi.org/10.1007/s10994-006-6226-1.

Grinsztajn, L., Oyallon, E., Varoquaux, G., 2024. Why do tree-based models still outperform deep learning on typical tabular data? NeurIPS 37, 507–520.

Grünhage, L., Jäger, H.-J., Haenel, H.-D., Löpmeier, F.-J., Hanewald, K., 1999. The European critical levels for ozone: improving their usage. Environ. Pollut. 105, 163–173. https://doi.org/10.1016/S0269-7491(99)00029-9.

Han, H., Liu, J., Shu, L., Wang, T., Yuan, H., 2020. Local and synoptic meteorological influences on daily variability in summertime surface ozone in eastern China. Atmos. Chem. Phys. 20, 203–222. https://doi.org/10.5194/acp-20-203-2020.

Han, S., Bian, H., Feng, Y., Liu, A., Li, X., Zeng, F., Zhang, X., 2011. Analysis of the relationship between $O_3$, NO, and $NO_2$ in Tianjin, China. Aerosol Air Qual. Res. 11, 128–139. https://doi.org/10.4209/aaqr.2010.07.0055.

Hayes, F., Bangor, C., 2017a. III. Mapping critical levels for vegetation. https://unece.org/fileadmin/DAM/env/documents/2017/AIR/EMEP/Final_new_Chapter_3_v2_August_2017_.pdfHayes.

He, K., Zhang, X., Ren, S., Sun, J., 2015. Deep Residual Learning for Image Recognition. The Computer Vision Foundation. https://www.cv-foundation.org/openaccess/content_cvpr_2016/papers/He_Deep_Residual_Learning_CVPR_2016_paper.pdf.

He, P., Xie, Z., Chi, X., Yu, X., Fan, S., Kang, H., Liu, C., Zhan, H., 2018. Atmospheric $\Delta^{17}O(NO_3^-)$ reveals nocturnal chemistry dominates nitrate production in Beijing haze. Atmos. Chem. Phys. 18, 14,465–14,476. https://doi.org/10.5194/acp-18-14465-2018.

He, Q., Ju, W., Dai, S., He, W., Song, L., Wang, S., Li, X., Mao, G., 2021. Drought risk of global terrestrial gross primary productivity over the last 40 years detected by a remote-sensing-driven process model. J. Geophys. Res. Biogeosci. 126. https://doi.org/10.1029/2020JG005944 e2020JG005944.

Heck, W.W., Cowling, E.B., 1997. The need for a long term cumulative secondary ozone standard - an ecological perspective. EM January, pp. 23–33.

Hinton, G.E., Osindero, S., Teh, Y.-W., 2006. A fast learning algorithm for deep belief nets. Neural Comput. 18, 1527–1554. https://doi.org/10.1162/neco.2006.18.7.1527.

Hou, T., Yu, S., Jiang, Y., Chen, X., Zhang, Y., Li, M., Li, Z., Song, Z., Li, P., Chen, J., Zhang, X., 2022. Impacts of chemical initial conditions in the WRF-CMAQ model on the ozone forecasts in eastern China. Aerosol Air Qual. Res. 22, 210402. https://doi.org/10.4209/aaqr.210402.

Hu, J., Chen, J., Ying, Q., Zhang, H., 2016. One-year simulation of ozone and particulate matter in China using WRF/CMAQ modeling system. Atmos. Chem. Phys. 16, 10,333–10,350. https://doi.org/10.5194/acp-16-10333-2016.

Hu, X.-M., Doughty, D.C., Sanchez, K.J., Joseph, E., Fuentes, J.D., 2012. Ozone variability in the atmospheric boundary layer in Maryland and its implications for vertical transport model. Atmos. Environ. 46, 354–364. https://doi.org/10.1016/j.atmosenv.2011.09.054.

Huang, X.-G., Zhao, J.-B., Cao, J.-J., Song, Y.-Y., 2019. Spatial-temporal variation of ozone concentration and its driving factors in China. Huan Jing Ke Xue 40, 1120–1131. https://doi.org/10.13227/j.hjkx.201807038.

Jia, A., Liang, S., Wang, D., Ma, L., Wang, Z., Xu, S., 2023. Global hourly, 5 km, all-sky land surface temperature data from 2011 to 2021 based on integrating geostationary and polar-orbiting satellite data. Earth Syst. Sci. Data 15, 869–895. https://doi.org/10.5194/essd-15-869-2023.

Jiang, Y.C., Zhao, T.L., Liu, J., Xu, X.D., Tan, C.H., Cheng, X.H., Bi, X.Y., Gan, J.B., You, J. F., Zhao, S.Z., 2015. Why does surface ozone peak before a typhoon landing in Southeast China? Atmos. Chem. Phys. 15, 13,331–13,338. https://doi.org/10.5194/acp-15-13331-2015.

Jin, X., Fiore, A.M., Murray, L.T., Valin, L.C., Lamsal, L.N., Duncan, B., Folkert Boersma, K., De Smedt, I., Abad, G.G., Chance, K., Tonnesen, G.S., 2017. Evaluating a space-based indicator of surface ozone-$NO_x$-VOC sensitivity over midlatitude source regions and application to decadal trends. J. Geophys. Res. Atmos. 122. https://doi.org/10.1002/2017JD026720.

Jin, Z., Yan, D., Zhang, Z., Li, M., Wang, T., Huang, X., Xie, M., Li, S., Zhuang, B., 2023. Effects of elevated ozone exposure on regional meteorology and air quality in China through ozone-vegetation coupling. J. Geophys. Res. Atmos. 128, e2022JD038119. https://doi.org/10.1029/2022JD038119.

Kang, Y., Choi, H., Im, J., Park, S., Shin, M., Song, C.-K., Kim, S., 2021. Estimation of surface-level $NO_2$ and $O_3$ concentrations using TROPOMI data and machine learning over East Asia. Environ. Pollut. 288, 117711. https://doi.org/10.1016/j.envpol.2021.117711.

Kangasjarvi, J., Jaspers, P., Kollist, H., 2005. Signalling and cell death in ozone-exposed plants. Plant Cell Environ. 28, 1021–1036. https://doi.org/10.1111/j.1365-3040.2005.01325.x.

Kavassalis, S.C., Murphy, J.G., 2017. Understanding ozone-meteorology correlations: a role for dry deposition. Geophys. Res. Lett. 44, 2922–2931. https://doi.org/10.1002/2016GL071791.

Ke, G., Meng, Q., Finley, T., Wang, T., Chen, W., Ma, W., Ye, Q., Liu, T.-Y., 2017. LightGBM: a highly efficient gradient boosting decision tree. In: Proceedings of the 31st International Conference on Neural Information Processing Systems, NIPS'17. Curran Associates Inc., Red Hook, NY, USA, pp. 3149–3157.

Kohut, R., 2007. Assessing the risk of foliar injury from ozone on vegetation in parks in the U.S. National Park Service's vital signs network. Environ. Pollut. 149, 348–357. https://doi.org/10.1016/j.envpol.2007.04.022.

Lefohn, A.S., Runeckles, V.C., 1987. Establishing standards to protect vegetation—ozone exposure/dose considerations. Atmos. Environ. 21, 561–568. https://doi.org/10.1016/0004-6981(87)90038-2.

Lei, C., Xu, X., Ma, Y., Jin, S., Liu, B., Gong, W., 2022. Full coverage estimation of the PM concentration across China based on an adaptive spatiotemporal approach. IEEE Trans. Geosci. Remote Sens. 60, 1–14. https://doi.org/10.1109/TGRS.2022.3213797.

Li, R., Wang, D., Wang, W., Nemani, R., 2023b. A GeoNEX-based high-spatiotemporal-resolution product of land surface downward shortwave radiation and photosynthetically active radiation. Earth Syst. Sci. Data 15, 1419–1436. https://doi.org/10.5194/essd-15-1419-2023.

Li, S., Wang, S., Wu, Q., Zhang, Y., Ouyang, D., Zheng, H., Han, L., Qiu, X., Wen, Y., Liu, M., Jiang, Y., Yin, D., Liu, K., Zhao, B., Zhang, S., Wu, Y., Hao, J., 2023c. Emission trends of air pollutants and $CO_2$ in China from 2005 to 2021. Earth Syst. Sci. Data Disc. 2023, 1–22. https://doi.org/10.5194/essd-2022-464.

Li, T., Cheng, X., 2021. Estimating daily full-coverage surface ozone concentration using satellite observations and a spatiotemporally embedded deep learning approach. Int. J. Appl. Earth Obs. 101, 102356. https://doi.org/10.1016/j.jag.2021.102356.

Li, T., Shen, H., Yuan, Q., Zhang, X., Zhang, L., 2017. Estimating ground-level $PM_{2.5}$ by fusing satellite and station observations: a geo-intelligent deep learning approach. Geophys. Res. Lett. 44, 11,985–11,993. https://doi.org/10.1002/2017GL075710.

Li, T., Wu, J., Chen, J., Shen, H., 2022. An enhanced geographically and temporally weighted neural network for remote sensing estimation of surface ozone. IEEE T. Geosci. Remote 60, 1–13. https://doi.org/10.1109/TGRS.2022.3187095.

Li, X., Ren, J., Huang, R., Chen, L., Li, Y., Qiao, X., Cheng, Y., Zhao, B., Yin, D., Gao, D., Sun, Y., Zhang, F., 2023a. The aggravation of summertime nocturnal ozone pollution in China and its potential impact on the trend of nitrate aerosols. Geophys. Res. Lett. 50, e2023GL103242. https://doi.org/10.1029/2023GL103242.

Liao, Z., Pan, Y., Ma, P., Jia, X., Cheng, Z., Wang, Q., Dou, Y., Zhao, X., Zhang, J., Quan, J., 2023. Meteorological and chemical controls on surface ozone diurnal variability in Beijing: a clustering-based perspective. Atmos. Environ. 295, 119566. https://doi.org/10.1016/j.atmosenv.2022.119566.

Lin, Y., Jiang, F., Zhao, J., Zhu, G., He, X., Ma, X., Li, S., Sabel, C.E., Wang, H., 2018. Impacts of $O_3$ on premature mortality and crop yield loss across China. Atmos. Environ. 194, 41–47. https://doi.org/10.1016/j.atmosenv.2018.09.024.

Liu, R., Ma, Z., Liu, Y., Shao, Y., Zhao, W., Bi, J., 2020. Spatiotemporal distributions of surface ozone levels in China from 2005 to 2017: a machine learning approach. Environ. Int. 142, 105823. https://doi.org/10.1016/j.envint.2020.105823.

Lu, X., Zhang, L., Zhao, Y., Jacob, D.J., Hu, Y., Hu, L., Gao, M., Liu, X., Petropavlovskikh, I., McClure-Begley, A., Querel, R., 2019. Surface and tropospheric ozone trends in the southern hemisphere since 1990: possible linkages to poleward expansion of the Hadley circulation. Sci. Bull. 64, 400–409. https://doi.org/10.1016/j.scib.2018.12.021.

Lundberg, S.M., Erion, G., Chen, H., DeGrave, A., Prutkin, J.M., Nair, B., Katz, R., Himmelfarb, J., Bansal, N., Lee, S.-I., 2020. From local explanations to global understanding with explainable AI for trees. Nat. Mach. Intell. 2, 56–67. https://doi.org/10.1038/s42256-019-0138-9.

Ma, R., Ban, J., Wang, Q., Zhang, Y., Yang, Y., He, M.Z., Li, S., Shi, W., Li, T., 2021. Random forest model based fine scale spatiotemporal $O_3$ trends in the Beijing-Tianjin-Hebei region in China, 2010 to 2017. Environ. Pollut. 276. https://doi.org/10.1016/j.envpol.2021.116635.

Ministry of Ecology and Environment (MEE), 2018. Revision of the Ambient Air Quality Standards (GB 3095–2012) (in Chinese) [WWW Document]. https://www.mee.gov.cn/gkml/sthjbgw/sthjbgg/201808/t20180815_451398.htm.

Morris, G.A., Ford, B., Rappenglück, B., Thompson, A.M., Mefferd, A., Ngan, F., Lefer, B., 2010. An evaluation of the interaction of morning residual layer and afternoon mixed layer ozone in Houston using ozonesonde data. Atmos. Environ. 44, 4024–4034. https://doi.org/10.1016/j.atmosenv.2009.06.057.

Niu, Y., Zhou, Y., Chen, R., Yin, P., Meng, X., Wang, W., Liu, C., Ji, J.S., Qiu, Y., Kan, H., Zhou, M., 2022. Long-term exposure to ozone and cardiovascular mortality in China: a nationwide cohort study. Lancet Planet. Health 6, e496–e503. https://doi.org/10.1016/S2542-5196(22)00093-6.

Pascanu, R., Mikolov, T., Bengio, Y., 2013. On the difficulty of training recurrent neural networks. Intern. Confer. Machine Learning. Pmlr 1310–1318. https://doi.org/10.48550/arXiv.1211.5063.

Proietti, C., Anav, A., De Marco, A., Sicard, P., Vitale, M., 2016. A multi-sites analysis on the ozone effects on gross primary production of European forests. Sci. Total Environ. 556, 1–11. https://doi.org/10.1016/j.scitotenv.2016.02.187.

Qiao, X., Guo, H., Wang, P., Tang, Y., Ying, Q., Zhao, X., Deng, W., Zhang, H., 2019. Fine particulate matter and ozone pollution in the 18 cities of the Sichuan Basin in southwestern China: model performance and characteristics. Aerosol Air Qual. Res. 19, 2308–2319. https://doi.org/10.4209/aaqr.2019.05.0235.

Ren, J., Guo, F., Xie, S., 2022. Diagnosing ozone–$NO_x$–VOC sensitivity and revealing causes of ozone increases in China based on 2013–2021 satellite retrievals. Atmos. Chem. Phys. 22, 15035–15047. https://doi.org/10.5194/acp-22-15035-2022.

Rodriguez, J.D., Perez, A., Lozano, J.A., 2010. Sensitivity analysis of k-fold cross-validation in prediction error estimation. IEEE Trans. Pattern Anal. Mach. Intell. 32, 569–575. https://doi.org/10.1109/TPAMI.2009.187.

Sagi, O., Rokach, L., 2018. Ensemble learning: a survey. WIREs Data Min. Knowl. Discov. 8. https://doi.org/10.1002/widm.1249.

Seinfeld, J.H., Pandis, S.N., 2016. Atmospheric Chemistry and Physics: From Air Pollution to Climate Change. John Wiley & Sons.

Shah, V., Jacob, D.J., Li, K., Silvern, R.F., Zhai, S., Liu, M., Lin, J., Zhang, Q., 2020. Effect of changing $NO_x$ lifetime on the seasonality and long-term trends of satellite-observed tropospheric $NO_2$ columns over China. Atmos. Chem. Phys. 20, 1483–1495. https://doi.org/10.5194/acp-20-1483-2020.

Shen, L., Jacob, D.J., Liu, X., Huang, G., Li, K., Liao, H., Wang, T., 2019. An evaluation of the ability of the ozone monitoring instrument (OMI) to observe boundary layer ozone pollution across China: application to 2005–2017 ozone trends. Atmos. Chem. Phys. 19, 6551–6560. https://doi.org/10.5194/acp-19-6551-2019.

Shinde, P.P., Shah, S., 2018. A review of machine learning and deep learning applications, in: 2018 fourth international conference on computing communication control and automation (ICCUBEA). In: Presented at the 2018 Fourth International Conference on Computing Communication Control and Automation (ICCUBEA), pp. 1–6. https://doi.org/10.1109/ICCUBEA.2018.8697857.

Song, G., Li, S., Xing, J., Yang, J., Dong, L., Lin, H., Teng, M., Hu, S., Qin, Y., Zeng, X., 2022. Surface UV-assisted retrieval of spatially continuous surface ozone with high spatial transferability. Remote Sens. Environ. 274, 112996. https://doi.org/10.1016/j.rse.2022.112996.

Stevenson, D.S., Young, P.J., Naik, V., Lamarque, J.-F., Shindell, D.T., Voulgarakis, A., Skeie, R.B., Dalsoren, S.B., Myhre, G., Berntsen, T.K., Folberth, G.A., Rumbold, S.T., Collins, W.J., MacKenzie, I.A., Doherty, R.M., Zeng, G., van Noije, T.P.C., Strunk, A., Bergmann, D., Cameron-Smith, P., Plummer, D.A., Strode, S.A., Horowitz, L., Lee, Y. H., Szopa, S., Sudo, K., Nagashima, T., Josse, B., Cionni, I., Righi, M., Eyring, V., Conley, A., Bowman, K.W., Wild, O., Archibald, A., 2013. Tropospheric ozone changes, radiative forcing and attribution to emissions in the atmospheric chemistry and climate model Intercomparison project (ACCMIP). Atmos. Chem. Phys. 13, 3063–3085. https://doi.org/10.5194/acp-13-3063-2013.

Strode, S.A., Ziemke, J.R., Oman, L.D., Lamsal, L.N., Olsen, M.A., Liu, J., 2019. Global changes in the diurnal cycle of surface ozone. Atmos. Environ. 199, 323–333. https://doi.org/10.1016/j.atmosenv.2018.11.028.

Stutz, J., Alicke, B., Ackermann, R., Geyer, A., Wang, S., White, A.B., Williams, E.J., Spicer, C.W., Fast, J.D., 2004. Relative humidity dependence of HONO chemistry in urban areas. J. Geophys. Res. Atmos. 109, 2003JD004135. https://doi.org/10.1029/2003JD004135.

Sun, H., Shin, Y.M., Xia, M., Ke, S., Wan, M., Yuan, L., Guo, Y., Archibald, A.T., 2022. Spatial resolved surface ozone with urban and rural differentiation during 1990-2019: a space-time Bayesian neural network downscaler. Environ. Sci. Technol. 56, 7337–7349. https://doi.org/10.1021/acs.est.1c04797.

Super, I., Vilà-Guerau de Arellano, J., Krol, M.C., 2015. Cumulative ozone effect on canopy stomatal resistance and the impact on boundary layer dynamics and $CO_2$ assimilation at the diurnal scale: a case study for grassland in the Netherlands. J. Geophys. Res. Biogeosci. 120, 1348–1365. https://doi.org/10.1002/2015JG002996.

Tong, D.Q., Mathur, R., Kang, D., Yu, S., Schere, K.L., Pouliot, G., 2009. Vegetation exposure to ozone over the continental United States: assessment of exposure indices by the eta-CMAQ air quality forecast model. Atmos. Environ. 43, 724–733. https://doi.org/10.1016/j.atmosenv.2008.09.084.

Valuntaitė, V., Valuntaitė, V., Šerevičienė, V., Girgždienė, R., Paliulis, D., 2012. Relative humidity and temperature impact to ozone and nitrogen oxides removal rate in the experimental chamber. J. Environ. Eng. Landsc. 20, 35–41. https://doi.org/10.3846/16486897.2011.633335.

Vaswani, A., Shazeer, N., Parmar, N., Uszkoreit, J., Jones, L., Gomez, A.N., Kaiser, L., Polosukhin, I., 2017. Attention is all you need. Adv. Neural Inf. Proces. Syst. 30. https://doi.org/10.48550/arXiv.1706.03762.

Wang, L., Zhu, H., Lin, A., Zou, L., Qin, W., Du, Q., 2017b. Evaluation of the latest MODIS GPP products across multiple biomes using global eddy covariance flux data. Remote Sens. 9, 418. https://doi.org/10.3390/rs9050418.

Wang, N., Guo, H., Jiang, F., Ling, Z.H., Wang, T., 2015. Simulation of ozone formation at different elevations in mountainous area of Hong Kong using WRF-CMAQ model. Sci. Total Environ. 505, 939–951. https://doi.org/10.1016/j.scitotenv.2014.10.070.

Wang, S., Mu, X., Jiang, P., Huo, Y., Zhu, L., Zhu, Z., Wu, Y., 2022a. New deep learning model to estimate ozone concentrations found worrying exposure level over eastern China. Int. J. Environ. Res. Public Health 19, 7186. https://doi.org/10.3390/ijerph19127186.

Wang, T., Xue, L., Brimblecombe, P., Lam, Y.F., Li, L., Zhang, L., 2017a. Ozone pollution in China: a review of concentrations, meteorological influences, chemical precursors, and effects. Sci. Total Environ. 575, 1582–1596. https://doi.org/10.1016/j.scitotenv.2016.10.081.

Wang, T., Xue, L., Feng, Z., Dai, J., Zhang, Y., Tan, Y., 2022b. Ground-level ozone pollution in China: a synthesis of recent findings on influencing factors and impacts. Environ. Res. Lett. 17, 063003. https://doi.org/10.1088/1748-9326/ac69fe.

Wang, Y., Gao, W., Wang, S., Song, T., Gong, Z., Ji, D., Wang, L., Liu, Z., Tang, G., Huo, Y., Tian, S., Li, J., Li, M., Yang, Y., Chu, B., Petäjä, T., Kerminen, V.-M., He, H., Hao, J., Kulmala, M., Wang, Yuesi, Zhang, Y., 2020. Contrasting trends of $PM_{2.5}$ and surface-ozone concentrations in China from 2013 to 2017. Natl. Sci. Rev. 7, 1331–1339. https://doi.org/10.1093/nsr/nwaa032.

Wang, Y., Yuan, Q., Li, T., Zhu, L., Zhang, L., 2021. Estimating daily full-coverage near surface $O_3$, CO, and $NO_2$ concentrations at a high spatial resolution over China based on S5P-TROPOMI and GEOS-FP. ISPRS J. Photogramm. Remote Sens. 175, 311–325. https://doi.org/10.1016/j.isprsjprs.2021.03.018.

Wang, Y., Yuan, Q., Zhu, L., Zhang, L., 2022c. Spatiotemporal estimation of hourly 2-km ground-level ozone over China based on Himawari-8 using a self-adaptive geospatially local model. Geosci. Front. 13, 101286. https://doi.org/10.1016/j.gsf.2021.101286.

Wei, J., Li, Z., Lyapustin, A., Sun, L., Peng, Y., Xue, W., Su, T., Cribb, M., 2021. Reconstructing 1-km-resolution high-quality $PM_{2.5}$ data records from 2000 to 2018 in China: spatiotemporal variations and policy implications. Remote Sens. Environ. 252, 112136. https://doi.org/10.1016/j.rse.2020.112136.

Wei, J., Li, Z., Li, K., Dickerson, R.R., Pinker, R.T., Wang, J., Liu, X., Sun, L., Xue, W., Cribb, M., 2022a. Full-coverage mapping and spatiotemporal variations of ground-level ozone ($O_3$) pollution from 2013 to 2020 across China. Remote Sens. Environ. 270, 112775. https://doi.org/10.1016/j.rse.2021.112775.

Wei, J., Liu, S., Li, Z., Liu, C., Qin, K., Liu, X., Pinker, R.T., Dickerson, R.R., Lin, J., Boersma, K.F., Sun, L., Li, R., Xue, W., Cui, Y., Zhang, C., Wang, J., 2022b. Ground-level $NO_2$ surveillance from space across China for high resolution using interpretable spatiotemporally weighted artificial intelligence. Environ. Sci. Technol. 56, 9988–9998. https://doi.org/10.1021/acs.est.2c03834.

Wei, J., Li, Z., Chen, X., Li, C., Sun, Y., Wang, J., Lyapustin, A., Brasseur, G.P., Jiang, M., Sun, L., Wang, T., Jung, C.H., Qiu, B., Fang, C., Liu, X., Hao, J., Wang, Y., Zhan, M., Song, X., Liu, Y., 2023. Separating daily 1 km $PM_{2.5}$ inorganic chemical composition in China since 2000 via deep learning integrating ground, satellite, and model data. Environ. Sci. Technol. 57, 18,282–18,295. https://doi.org/10.1021/acs.est.3c00272.

Wei, J., Wang, Z., Li, Z., Li, Z., Pang, S., Xi, X., Cribb, M., Sun, L., 2024. Global aerosol retrieval over land from Landsat imagery integrating transformer and Google earth engine. Remote Sens. Environ. 315, 114404. https://doi.org/10.1016/j.rse.2024.114404.

WHO global air quality guidelines, 2021. Particulate Matter ($PM_{2.5}$ and $PM_{10}$), Ozone, Nitrogen Dioxide, Sulfur Dioxide and Carbon Monoxide. https://www.who.int/publications/i/item/9789240034228.

Wilkinson, S., Mills, G., Illidge, R., Davies, W.J., 2012. How is ozone pollution reducing our food supply? J. Exp. Bot. 63, 527–536. https://doi.org/10.1093/jxb/err317.

Xia, Y., Hu, Y., Huang, Y., Bian, J., Zhao, C., Wei, J., Yan, Y., Xie, F., Lin, J., 2022. Concurrent hot extremes and high ultraviolet radiation in summer over the Yangtze plain and their possible impact on surface ozone. Environ. Res. Lett. 17, 064001. https://doi.org/10.1088/1748-9326/ac6c3c.

Xie, S., Girshick, R., Dollár, P., Tu, Z., He, K., 2017. Aggregated Residual Transformations for Deep Neural Networks. Computer Vision Foundation. https://openaccess.thecvf.com/content_cvpr_2017/papers/Xie_Aggregated_Residual_Transformations_CVPR_2017_paper.pdf.

Xu, J., Xu, X., Lin, W., Ma, Z., Ma, J., Wang, R., Wang, Y., Zhang, G., Xu, W., 2020. Understanding the formation of high-ozone episodes at Raoyang, a rural site in the north China plain. Atmos. Environ. 240, 117797. https://doi.org/10.1016/j.atmosenv.2020.117797.

Xu, J., Huang, X., Wang, N., Li, Y., Ding, A., 2021. Understanding ozone pollution in the Yangtze River Delta of eastern China from the perspective of diurnal cycles. Sci. Total Environ. 752, 141928. https://doi.org/10.1016/j.scitotenv.2020.141928.

Xue, T., Zheng, Y., Geng, G., Xiao, Q., Meng, X., Wang, M., Li, X., Wu, N., Zhang, Q., Zhu, T., 2020. Estimating spatiotemporal variation in ambient ozone exposure during 2013–2017 using a data-fusion model. Environ. Sci. Technol. 54, 14,877–14,888. https://doi.org/10.1021/acs.est.0c03098.

Xue, W., Zhang, J., Hu, X., Yang, Z., Wei, J., 2022. Hourly seamless surface $O_3$ estimates by integrating the chemical transport and machine learning models in the Beijing-Tianjin-Hebei region. Int. J. Environ. Res. Public Health 19, 8511. https://doi.org/10.3390/ijerph19148511.

Yamashita, R., Nishio, M., Do, R.K.G., Togashi, K., 2018. Convolutional neural networks: an overview and application in radiology. Insights Imag. 9, 611–629. https://doi.org/10.1007/s13244-018-0639-9.

Yu, W., Ye, T., Zhang, Yiwen, Xu, R., Lei, Y., Chen, Z., Yang, Z., Zhang, Yuxi, Song, J., Yue, X., Li, S., Guo, Y., 2023. Global estimates of daily ambient fine particulate matter concentrations and unequal spatiotemporal distribution of population exposure: a machine learning modelling study. Lancet Planet. Health 7, e209–e218. https://doi.org/10.1016/S2542-5196(23)00008-6.

Yu, Y., Si, X., Hu, C., Zhang, J., 2019. A review of recurrent neural networks: LSTM cells and network architectures. Neural Comput. 31, 1235–1270. https://doi.org/10.1162/neco_a_01199.

Yue, X., Unger, N., 2014. Ozone vegetation damage effects on gross primary productivity in the United States. Atmos. Chem. Phys. 14, 9137–9153. https://doi.org/10.5194/acp-14-9137-2014.

Zhan, Y., Luo, Y., Deng, X., Grieneisen, M.L., Zhang, M., Di, B., 2018. Spatiotemporal prediction of daily ambient ozone levels across China using random forest for human exposure assessment. Environ. Pollut. 233, 464–473. https://doi.org/10.1016/j.envpol.2017.10.029.

Zhang, T., Wu, Y., Guo, Y., Yan, B., Wei, J., Zhang, H., Meng, X., Zhang, C., Sun, H., Huang, L., 2022. Risk of illness-related school absenteeism for elementary students with exposure to $PM_{2.5}$ and $O_3$. Sci. Total Environ. 842, 156824. https://doi.org/10.1016/j.scitotenv.2022.156824.

Zhang, W., Liu, D., Tian, H., Pan, N., Yang, R., Tang, W., Yang, J., Lu, F., Dayananda, B., Mei, H., Wang, S., Shi, H., 2024. Parsimonious estimation of hourly surface ozone concentration across China during 2015–2020. Sci. Data 11, 492. https://doi.org/10.1038/s41597-024-03302-3.

Zhang, Y., Wang, W., He, J., Jin, Z., Wang, N., 2023. Spatially continuous mapping of hourly ground ozone levels assisted by Himawari-8 short wave radiation products. Gisci. Remote Sens. 60. https://doi.org/10.1080/15481603.2023.2174280.

Zhao, W., Fan, S., Guo, H., Gao, B., Sun, J., Chen, L., 2016. Assessing the impact of local meteorological variables on surface ozone in Hong Kong during 2000–2015 using quantile and multiple line regression models. Atmos. Environ. 144, 182–193. https://doi.org/10.1016/j.atmosenv.2016.08.077.

Zhou, Z.-H., Feng, J., 2019. Deep forest. Natl. Sci. Rev. 6, 74–86. https://doi.org/10.1093/nsr/nwy108.

Zhu, S., Xu, J., Zhu, H., Zeng, J., Wang, Y., Zeng, Q., Zhang, D., Liu, X., Yang, S., 2022. Investigating impacts of ambient air pollution on the terrestrial gross primary productivity (GPP) from remote sensing. IEEE Geosci. Remote Sens. 19, 1–5. https://doi.org/10.1109/LGRS.2022.3163775.

Zhu, S., Xu, J., Zeng, J., Yu, C., Wang, Y., Wang, H., Shi, J., 2023. LESO: a ten-year ensemble of satellite-derived intercontinental hourly surface ozone concentrations. Sci. Data 10, 741. https://doi.org/10.1038/s41597-023-02656-4.